remote sensing

MDPI

Article

Spatiotemporal Dynamics and Driving Patterns of Forest Fires in Yunnan Province, China: An Empirical Study Based on Event-Level Reconstruction from Multi-Source Remote Sensing (2012–2024)

Hang Deng, Junfan Zhao, Lan Wang and Fan Zhao *

School of Big Data and Intelligent Engineering, Southwest Forestry University, Kunming 650224, China; denghang@swfu.edu.cn (H.D.); zhaojunfan033@163.com (J.Z.); m18760227697@163.com (L.W.)
* Correspondence: fzhao@swfu.edu.cn

Highlights

What are the main findings?

- Starting from 497,834 raw Active Fire Spots (AFSs) detected during 2012–2024, we identified 41,215 validated FFEs through optical–thermal screening, spatio-temporal clustering, and event-level validation.
- Fire activity in Yunnan showed clear temporal, spatial, and topographic heterogeneity: 32.8% of all FFEs were concentrated in the late dry season, daytime fires accounted for 82.8% of all FFEs, and nighttime fires were centered 215.03 m higher than daytime fires.

What are the implications of the main findings?

- Event-level reconstruction provides a more informative basis than AFS counts alone for understanding fire heterogeneity in fragmented mountainous environments, because it links occurrence, persistence, CFRP, BA, and AGB loss within physically independent FFEs.
- The results support zone-specific fire management in Yunnan: frequent escaped fires in basin agroforestry ecotones require stronger ignition prevention and rapid suppression, whereas conifer-dominated uplands and deeply incised valleys require greater attention to high-impact, persistent, and topographically constrained fires.

Abstract

Pixel-based Active Fire Spot (AFS) statistics alone are insufficient for characterizing forest fire activity in fragmented mountainous agroforestry regions because cross-sensor differences, geometric distortion, and discontinuous satellite overpasses can fragment physically continuous fires into multiple detections. To address this problem, we developed a reconstruction framework that combines optical–thermal cross-validation with multi-level spatio-temporal clustering to identify physically independent fires in Yunnan Province, China. Starting from 497,834 raw AFSs detected during 2012–2024, the framework removed unusable detections, aggregated the retained AFSs, and identified 41,215 validated Forest Fire Events (FFEs). The reconstructed database revealed clear temporal, spatial, and topographic heterogeneity. Fire activity was strongly concentrated in the late dry season, with 32.8% of all FFEs occurring during the main spring fire window. Daytime FFEs accounted for 82.8% of all FFEs, but nocturnal activity increased substantially in some years, reaching 20.7% in 2023. Persistence showed a long-tailed structure under both observation frameworks, although the operational thresholds differed between 2012–2017 (105 min)

Check for updates

Academic Editor: Nikos Koutsias

Received: 11 March 2026
Revised: 21 April 2026
Accepted: 23 April 2026
Published: 28 April 2026

Copyright: © 2026 by the authors. Licensee MDPI, Basel, Switzerland. This article is an open access article distributed under the terms and conditions of the Creative Commons Attribution (CC BY) license.

and 2018–2024 (75 min). Regionally, Southeast and Southwest Yunnan concentrated most reconstructed FFEs, whereas Northwest and Central Yunnan showed much higher CFRP per event. Topographically, fire energy was concentrated mainly on gentle-to-moderate slopes, and nighttime fires were centered 215.03 m higher than daytime fires. The typology analysis further showed that event frequency and physical fire impact were not distributed proportionally across fire types. Random Forest validation indicated high reproducibility of the rule-based typology system (Macro-F1 = 0.9935; Weighted-F1 = 0.9964), whereas the first two principal components explained 42.65% of the total variance. These results show that event-level reconstruction provides a stronger basis than AFS counts alone for understanding fire heterogeneity and supporting zone-specific fire management in Yunnan.

Keywords: forest fire; event-level reconstruction; multi-source remote sensing; fire dynamics; Yunnan; China

1. Introduction

Forest fires are a critical natural disturbance in terrestrial ecosystems and play an important role in vegetation succession, carbon cycling, and climate feedback processes [1–3]. Since the beginning of the 21st century, under the combined influence of extreme climate events and intensifying human activity, global wildfire activity has shown substantial increases in occurrence, spread scale, and Fire Radiative Power (FRP) [4–8]. In many fire-prone regions, prolonged drought, rising temperature, and altered fire-weather conditions have increased the probability of large and high-impact fires, while also amplifying their ecological and social consequences [4–6].

Recent studies have further shown that forest fire regimes in Yunnan and southwestern China are being increasingly reshaped by climate change, hydroclimatic anomalies, and changing fire-weather conditions [9–11]. In particular, modeling and observational evidence suggests that rising temperature, prolonged dry periods, shifts in humidity and wind regimes, and terrestrial water-storage anomalies can jointly intensify seasonal forest fire risk and alter the temporal structure of forest fire activity in Yunnan [9,10]. At longer timescales, forest fire occurrence in southwestern China has also been linked to the combined influence of climate variability and human activity, highlighting the need to interpret present-day forest fire dynamics within a broader climate–human coupling framework [11]. In this context, understanding not only where and when fires occur, but also how individual Forest Fire Events (FFEs) develop, persist, and produce heterogeneous ecological consequences, has become increasingly important for fire-risk assessment and regional fire management.

Against this background, geographically and climatically heterogeneous alpine-gorge regions have become important areas for fire dynamics research because of their complex environmental settings. Yunnan Province is not only a global biodiversity hotspot and a critical ecological barrier, but also a representative region in which climate, topography, vegetation, and human activity interact strongly [12,13]. Constrained by the rugged Hengduan Mountains and long-term agricultural reclamation, the province has developed a highly fragmented landscape pattern, ranging from flat upland basins to deeply incised river valleys and steep mountain slopes [12,14]. Existing studies have shown that meteorological fluctuations, such as relative humidity deficits, together with frequent agricultural production activities, are major drivers of forest fires in this region [13,15,16]. However, under such a multidimensional and heterogeneous fire system, conventional analyses based on administrative units or coarse spatial grids often struggle to delineate the physical boundaries of actual fire scars and to capture the uneven ecological consequences of fire spread across contrasting habitats.

A major part of this limitation lies in the mismatch between complex fire environments and pixel-based monitoring by polar-orbiting satellites. Large-scale analyses of fire activity have long relied on moderate-resolution active-fire products [17,18]. However, when used alone, MODIS-based AFS statistics face several well-known constraints. The actual observation footprint of a satellite pixel may be enlarged by scan geometry, especially near the swath edge, and such geometric distortion can become more problematic in mountainous terrain. In these environments, enlarged footprints may miss low-intensity smoldering fires, while mixed backgrounds, strong thermal convection, and smoke-related anomalies may also increase false detections [18,19]. The introduction of VIIRS products, which are more sensitive to smaller fires and have finer spatial resolution, has therefore improved the observation of fire activity in complex landscapes [20]. At the same time, the combined use of multiple polar-orbiting sensors has shortened the effective revisit interval, but has also introduced new challenges because different sensors differ in confidence systems, radiometric response, and spatial characteristics. As a result, simply merging multi-source AFSs can fragment a physically continuous fire into multiple detections and can bias estimates of FFEs frequency, Burned Area (BA), and FRP [21–23].

For this reason, reconstructing discrete active fire detections into physically independent FFEs has become an important direction in recent fire remote-sensing research [21,24,25]. In recent years, wildfire studies have increasingly shifted from pixel-based AFS statistics toward event-oriented reconstruction and tracking. For example, VIIRS-based spatio-temporal clustering has been used to improve fire-event delineation [25], object-based tracking systems have been applied to reconstruct the temporal evolution and spread of individual fires [21], and recent ST-DBSCAN-based approaches have further shown the value of integrating spatio-temporal clustering with radiative and burn-related metrics at the event scale [24]. These advances demonstrate the methodological importance of moving beyond isolated AFS counts toward physically meaningful FFEs. However, they have been applied mainly in relatively homogeneous settings or within single-sensor workflows. Fewer studies have addressed event reconstruction in highly fragmented mountainous agroforestry mosaics, where geometric distortion, cross-sensor differences, and discontinuous satellite overpasses can jointly affect FFEs counts, BA estimation, and FRP accounting.

In parallel, recent studies have also advanced the use of machine learning and related data-driven methods for burned-area mapping, fire-risk prediction, and fire-environment analysis in China and other fire-prone regions [12–14]. These approaches have improved the identification of burned scars, the prediction of seasonal fire risk, and the integration of multiple environmental drivers [12–14]. However, they have focused more on risk zonation, susceptibility modeling, or post-fire mapping than on reconstructing physically independent FFEs from fragmented multi-source AFS detections. This limitation is especially important in highly heterogeneous mountainous agroforestry mosaics such as Yunnan, where event fragmentation, cross-sensor inconsistency, and complex terrain can jointly bias hotspot-based fire statistics. Therefore, a more robust event-level framework is still needed to bridge the methodological gap between AFS detection, burned-scar verification, and physically meaningful fire-event reconstruction.

To address this gap, this study develops an event-level reconstruction framework for Yunnan Province that integrates optical–thermal cross-validation, multi-source spatio-temporal clustering, and morphological reconstruction [21,24,25]. Using long-term (2012–2024) active-fire products together with 30 m burned-area, biomass, and land cover type datasets, the framework reconstructs validated FFEs and links them to BA, affected Above-Ground Biomass (AGB), and Cumulative Fire Radiative Power (CFRP). Following recent advances in fire-event reconstruction, we implement a Multi-level Spatio-

Temporal Density-Based Spatial Clustering of Applications with Noise (MST-DBSCAN) to reorganize the life cycles of discrete fire detections, and combine this procedure with boundary morphology algorithms to resolve topological adhesion among adjacent fire scars [21,24,25]. In this way, the study moves beyond single-source pixel statistics and provides a more physically coherent basis for analyzing fire dynamics in a geographically complex and human-influenced mountain region.

Based on the reconstructed long-term, province-wide event database, this study addresses the following three questions.

(1) Methodological reconstruction and multi-source integration: How can optical–thermal cross-validation and event-level spatio-temporal clustering improve the reconstruction of independent FFEs from fragmented multi-source AFS detections in complex terrain?
(2) Temporal dynamics and frequency–impact mismatch: Under strong interannual climate variability, do forest fires in Yunnan exhibit a mismatch between event frequency and physical fire impact, such that relatively infrequent fire types contribute disproportionately to BA, CFRP, or AGB loss? How are these patterns expressed across seasonal, diurnal, and elevational dimensions?
(3) Topographic and habitat-related heterogeneity: How do topography and heterogeneous landscape settings, such as basin margins, sloping cropland, and deeply incised river valleys, influence the spatial organization and ecological consequence of FFEs?

Through event-level reconstruction of forest fire activity, this study aims to improve understanding of spatiotemporal fire dynamics and habitat-related fire consequences in the complex mountainous regions of Southwest China. More broadly, it seeks to provide an empirical basis for differentiated forest fire management and for future application of event-level reconstruction methods in other geographically complex fire-prone regions.

2. Materials and Methods

2.1. Study Area

The study area is Yunnan Province (21°09′–29°15′N, 97°30′–106°12′E), located on the southwestern frontier of China. It spans a total area of 394,100 km^2, with plateaus and mountains occupying over 90% of its territory, and forest coverage reaching approximately 60%. The terrain descends in a stepped pattern from the northwest (Meili Snow Mountain, 6740 m) to the southeast (Honghe River Valley, 76.4 m), with an average elevation of approximately 2000 m. This topography forms a typical highland mountainous landscape (Figure 1a). The region encompasses four climatic zones—tropical, subtropical, temperate, and cold—and is inhabited by 26 ethnic minority groups.

Based on natural geographical features, Yunnan is broadly divided into five zones, as shown in Figure 1b: Northeast Yunnan is dominated by fragmented highland terrain with sparse vegetation; Southeast Yunnan exhibits typical karst landscapes with ecologically fragile environments; Central Yunnan enjoys a mild climate and is the province's population and economic center; Northwest Yunnan comprises alpine gorges dominated by cold-temperate coniferous forests; and Southwest Yunnan features mountainous river valleys with well-developed tropical rainforests. The region's complex geomorphology and distinctive climate conditions lead to uneven spatial climate distribution, giving rise to localized microclimates. Together with rich biodiversity, diverse geo-climatic settings, extensive forest–agriculture interfaces, and recurrent agricultural burning activities, these characteristics make Yunnan a highly fire-prone and spatially heterogeneous region. Human-modified forest interfaces and settlement-adjacent landscapes are therefore important contexts for understanding wildfire risk and fire management in the province.

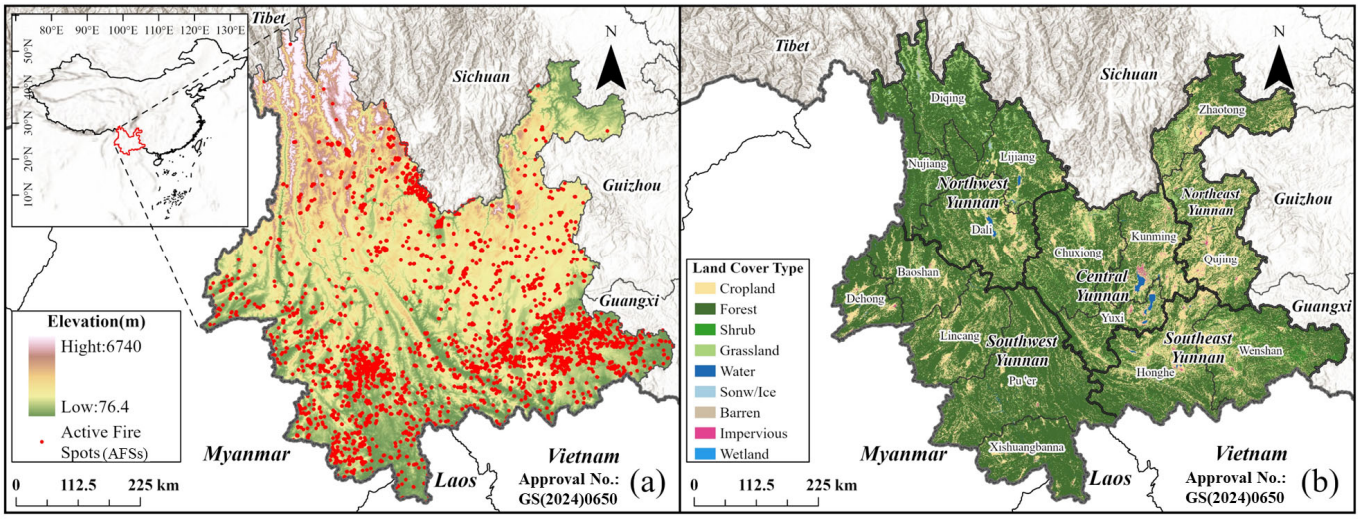


Figure 1. (**a**) Location of the study area and distribution of MODIS AFSs in 2020 (Type = 0). (**b**) Land cover types, geographical characteristics, and administrative divisions of Yunnan Province in 2020 based on CLCD (Northeast Yunnan includes: Zhaotong, Qujing; Southeast Yunnan includes: Wenshan, Honghe; Central Yunnan includes: Kunming, Yuxi, Chuxiong; Northwest Yunnan includes: Dali, Lijiang, Nujiang, Diqing; Southwest Yunnan includes: Pu'er, Xishuangbanna, Dehong, Baoshan, Lincang).

2.2. Data Sources

Active Fire (AF) data: Compared to active fire data collected by local authorities—which are often constrained by limited human and material resources, resulting in incomplete and difficult-to-acquire datasets—the MODIS MCD14ML and the VIIRS (VNP14IMG/VJ114IMG) AF product, freely provided by the NASA FIRMS platform, offers a longer temporal span and moderate spatiotemporal resolution. This product has been widely cross-validated in wildfire studies at both regional and global scales [15,16]. The data are currently stored in a standard-processed (Level-2) vector format (Table 1), comprising the geographic coordinates of AFS and their associated attribute information (Table 1). Each data point represents one or more fires occurring within the sensor's spatial footprint. Under ideal observation conditions, the algorithm can detect small-scale fires of 50–100 m^2 [17], thereby providing long-term, standardized data support for analyzing the spatiotemporal characteristics of forest fires globally.

Table 1. Details of active fire products.

Field Name	MCD14ML	VNP14IMG	VJ114IMG
satellite	Aqua and Terra	S-NPP	NOAA-20
instrument	MODIS	VIIRS	VIIRS
version	MODIS Collection 6.1	VIIRS Collection 2.0	VIIRS Collection 2.0
confidence	range: 0–100%	range: high, normal, low	range: high, normal, low
type	0: presumed vegetation fire; 1: active volcano; 2: other static; 3: offshore		
algorithm	Day/night algorithm switching flag: Day (D) or Night (N)		
latitude	Latitude of Active Fire Spots		
longitude	Longitude of Active Fire Spots		
scan	Actual pixel size along the scan direction		
track	Actual pixel size along the track direction		
acq_date	Get the date of the Active Fire Spots		
acq_time	Time to get Active Fire Spots		
frp	Fire Radiative Power		

Burned Area (BA) data: The Global Annual Burned Area Maps (GABAM) is an automated dataset of BA data generated using nearly all available Landsat imagery on the Google Earth Engine (GEE) platform. It provides free access to 30 m annual BA data for most regions of the world from 2000 to 2021 (covering the range 180°W–180°E and 80°N–60°S), with detailed information available in Table 2. This dataset demonstrates a similar spatial distribution and strong correlation when compared with the BA in the Fire_CCI 5.0 product. In global stratified sampling validation, the commission errors and omission errors of GABAM were 13.17% and 30.13%, respectively, with global accuracy exceeding 90% [18].

Table 2. Description of multi-source remote sensing data and parameters used in this study.

Data Type	Product Name	Earth Observation Platforms	Spatial Res.	Temporal Res.	Data Source
Active Fire	MCD14ML	Terra and Aqua	~1000 m	2012–2024; Daily	https://firms.modaps.eosdis.nasa.gov (accessed on 22 April 2026)
	VNP14IMG	Suomi-NPP	~375 m	2012–2024; Daily	
	VJ114IMG	NOAA-20	~375 m	2018–2024; Daily	
Burned Area	GABAM	Landsat Series	30 m	2012–2024; Annual	https://zenodo.org/records/17707433 (accessed on 22 April 2026)
Biomass	CFATD	Landsat Series	30 m	2012–2023; Annual	https://zenodo.org/records/12742210 (accessed on 22 April 2026)
Topography	DEM	Space Shuttle	~30 m	2020; Static	https://earthexplorer.usgs.gov (accessed on 22 April 2026)
Land Cover Type	CLCD	Landsat Series	30 m	2012–2024; Annual	https://zenodo.org/records/5210928 (accessed on 22 April 2026)

Land Cover Type (LCT) data: The China Land Cover Dataset (CLCD) is a dataset used to describe Land Cover Types and their spatial distribution in China from 1985 to 2023. It is also jointly developed and regularly updated based on the GEE platform, with high temporal and spatial consistency [19]. It includes nine major land cover types: Cropland, Forest, Shrub, Grassland, Water, Snow/Ice, Barren, Impervious, and Wetland, as shown in Figure 1.

Above-Ground Biomass (AGB) data: As the first dataset dedicated to monitoring forest AGB in China, the China Annual Forest Above-Ground Biomass Time-Series Dataset (CFATD) provides 30 m resolution annual AGB density estimates from 1985 to 2023. With values expressed in megagrams per hectare (Mg/ha) per pixel, it enables the precise quantification of tree cover and the detection of dynamic changes within each landscape pixel.

2.3. Data Processing Methods

To reconstruct real and independent FFEs in complex mountainous terrain, we developed an event-level framework using ArcGIS Pro 3.5.3 and Python 3.11.14 to integrate fragmented multi-source satellite fire detections from 2012 to 2024 into FFEs with coherent life cycles. The workflow consists of four steps. First, likely vegetation-fire detections were identified from multi-source active fire products, while obvious non-target thermal anomalies were removed using land-cover information. Second, the actual detection footprints of the fire pixels were reconstructed according to the observation geometry of each sensor and cross-validated against the corresponding burned-area data to reduce false or spatially inconsistent detections. Third, the retained multi-source fire detections were

grouped through multi-level spatiotemporal clustering, so that observations from different sensors, overpass times, and spatial resolutions could be integrated into the same FFEs. Finally, morphological reconstruction was used to extract event-level burned area and to further link AGB loss through land-cover context, thereby generating an event-level database for analyzing the spatiotemporal dynamics of forest fires. The main workflow is shown in Figure 2.

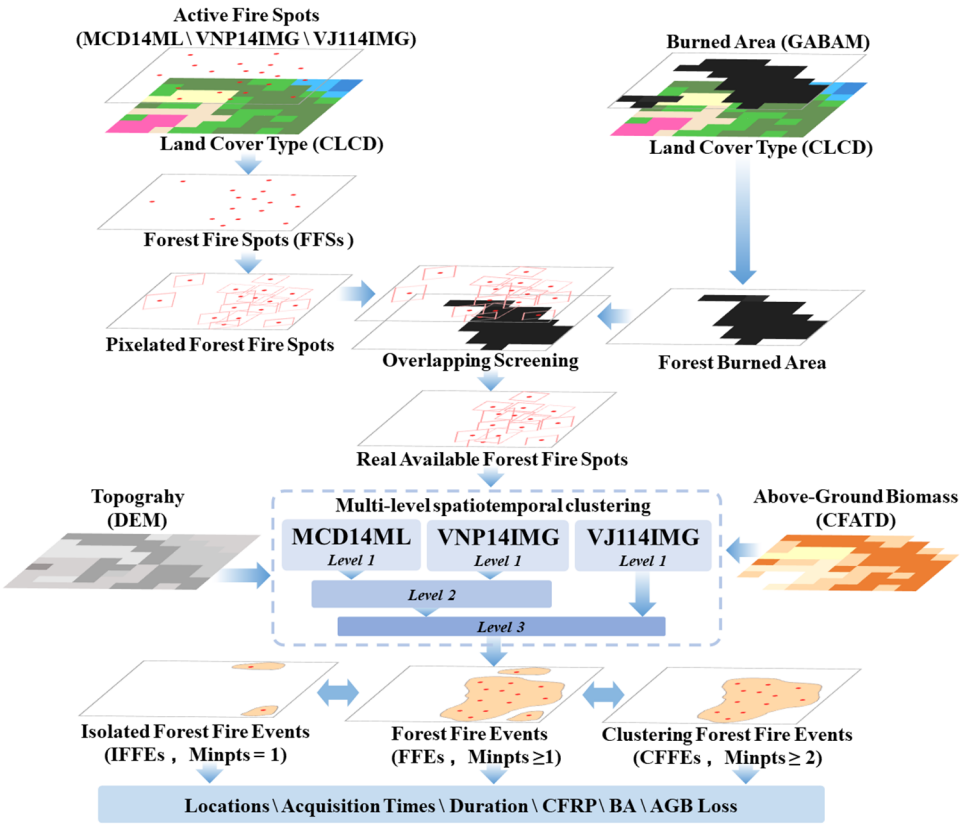


Figure 2. Flowchart of the methodology used in this study. Each sub-pixel of the land cover type (CLCD), topography (DEM), above-ground biomass (AGB), and burned area (BA) layers measures 30 m × 30 m. The colors and red dots are used to distinguish different data layers, spatial features, and fire spots in the workflow. For layers with categorical or quantitative meanings, the colors follow the corresponding data attributes; otherwise, they are used only for schematic visualization. The pixelation of FFSs is illustrative only and does not represent their actual pixel size.

First, to maximize the retention of potential wildfire information, this study extracted presumed vegetation fire spots across all confidence levels (TYPE = 0). In conjunction with LCT data, AFSs spatially located within pixels classified as forest, shrubland, grassland, and cropland (inclusive of forest fires triggered by escaped agricultural fires) [20] were uniformly reclassified as FFSs. Thermal anomalies in non-target land cover types, such as urban areas, were strictly excluded.

Second, to overcome the geometric distortion of polar-orbiting satellites and improve the spatial matching accuracy among multi-source data, this study conducted a pixelation restoration of the initial AFSs based on the metadata fields (TRACK and SCAN) of the fire products from each satellite source [21,22]. This step reconstructed the geometric topological boundaries of their instantaneous observations, thereby restoring the actual pixel footprint coverage of MODIS and VIIRS when detecting surface thermal anomalies (Figure 3). This provided an accurate spatial benchmark for the subsequent BA pixel matching.

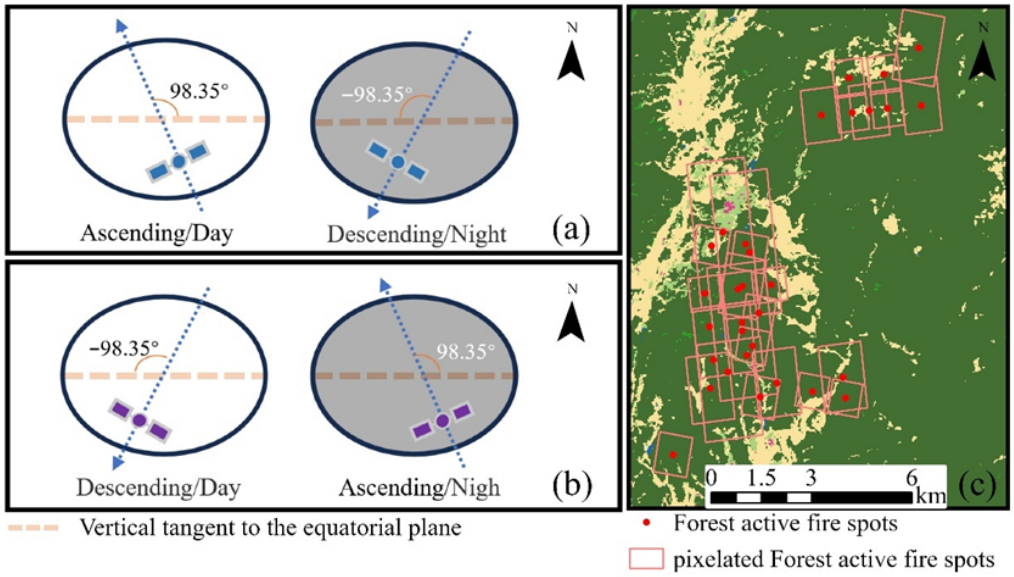


Figure 3. (**a**) Schematic illustration of the inclination angle between the Aqua satellite's orbit and the equatorial plane. (**b**) Schematic illustration of the inclination angle between the Terra satellite's orbit and the equatorial plane. (**c**) Pixelized forest AFSs. Blue and purple symbols represent Aqua and Terra examples, respectively; red dots indicate forest AFSs; red frames indicate pixelized forest AFSs; and background colors in panel (**c**) indicate land-cover classes.

Subsequently, during the spatial co-selection phase of AFS and BA data, this study introduced a cross-validation mechanism based on 'thermal-optical characteristics' [17,22,23]. On the one hand, it eliminated 'pseudo-burned area' pixels erroneously generated by optical remote sensing (BA) due to interference from mountain shadows, cloud shadows, and seasonal deciduous leaf fall in complex terrains (Figure 4a,b). On the other hand, it stripped away abnormal heat sources lacking the physical imprint of a continuous burned surface (e.g., 'fire-without-scar' AFSs caused by agricultural fire spillover, Figure 4c). Ultimately, only highly reliable AFSs possessing both authentic thermal radiation seeds and continuous physical burn scars were retained (Figure 4d), which effectively eliminated the inherent false-positive errors of single-source data.

Constrained by the discontinuous overpasses and sensor-specific observation characteristics of polar-orbiting satellites, a spatially continuous fire may be represented by multiple AFS segments detected at different times and by different sensors [21,26]. To mitigate this "time-slicing" effect caused by discontinuous observations, we adopted Spatio-Temporal Density-Based Spatial Clustering of Applications with Noise (ST-DBSCAN) as the core event-aggregation algorithm. Because this clustering procedure was implemented sequentially across multiple sensor-combination levels (single-satellite source, VIIRS-only integration, and all-satellite-source integration), we refer to the final framework hereafter as Multi-level ST-DBSCAN (MST-DBSCAN). The core purpose of this strategy is to re-assimilate multi-source, discrete, and locally observed AFSs through spatio-temporal density clustering, thereby reconstructing them into complete and physically independent FFEs. At the algorithm execution level, clustering was advanced hierarchically following the sequence of "single-satellite source, VIIRS, and all-satellite sources". The core parameters were set as follows: spatial neighborhood threshold (MODIS Eps = 1450 m; VIIRS Eps = 550 m), temporal neighborhood threshold ($\Delta t = 7$ d), and core point density threshold (MinPts = 2). Consequently, discrete pixels were aggregated into FFEs with independent lifecycles. The output FFEs were classified into two categories: persistent fires mixed from multi-source data (MinPts ≥ 2) and isolated short-term fires captured by a single satellite source (MinPts = 1). For the latter, an empirical burning duration (75–105 min) derived

from the integration of multiple satellite sources was further assigned to complete their temporal evolution characteristics.

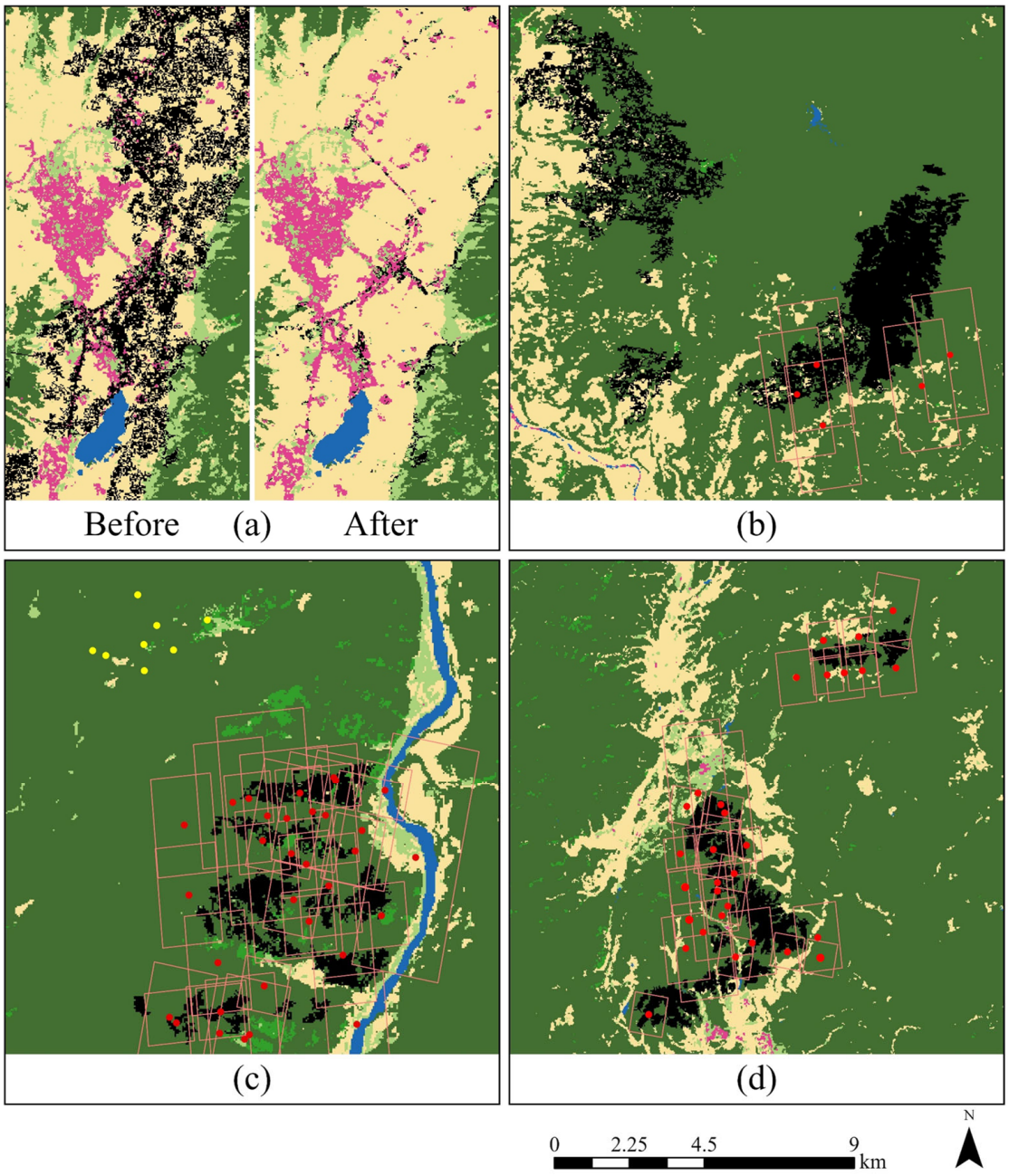


Figure 4. Screening and pixelation of forest active fire spots (AFSs). (**a**) Comparison before and after removing misclassified farmland/bare-soil areas. (**b**) Misclassified burned-area (BA) pixels within forest areas. (**c**) Forest AFSs located within forest areas but excluded as unavailable; yellow dots indicate excluded forest AFSs. (**d**) Final retained forest AFSs after screening. Background colors indicate land-cover classes, black patches indicate BA pixels, red dots indicate forest AFSs, and red frames indicate pixelated forest AFS footprints.

Finally, addressing the common issues of excessive adhesion or fragmented omissions in BA within complex mountainous environments, this study developed an adaptive morphological reconstruction algorithm comprising three core modules. This aims to accurately match and extract the true event-level BA, as well as its corresponding 30 m forest AGB and land cover type (Figure 5).

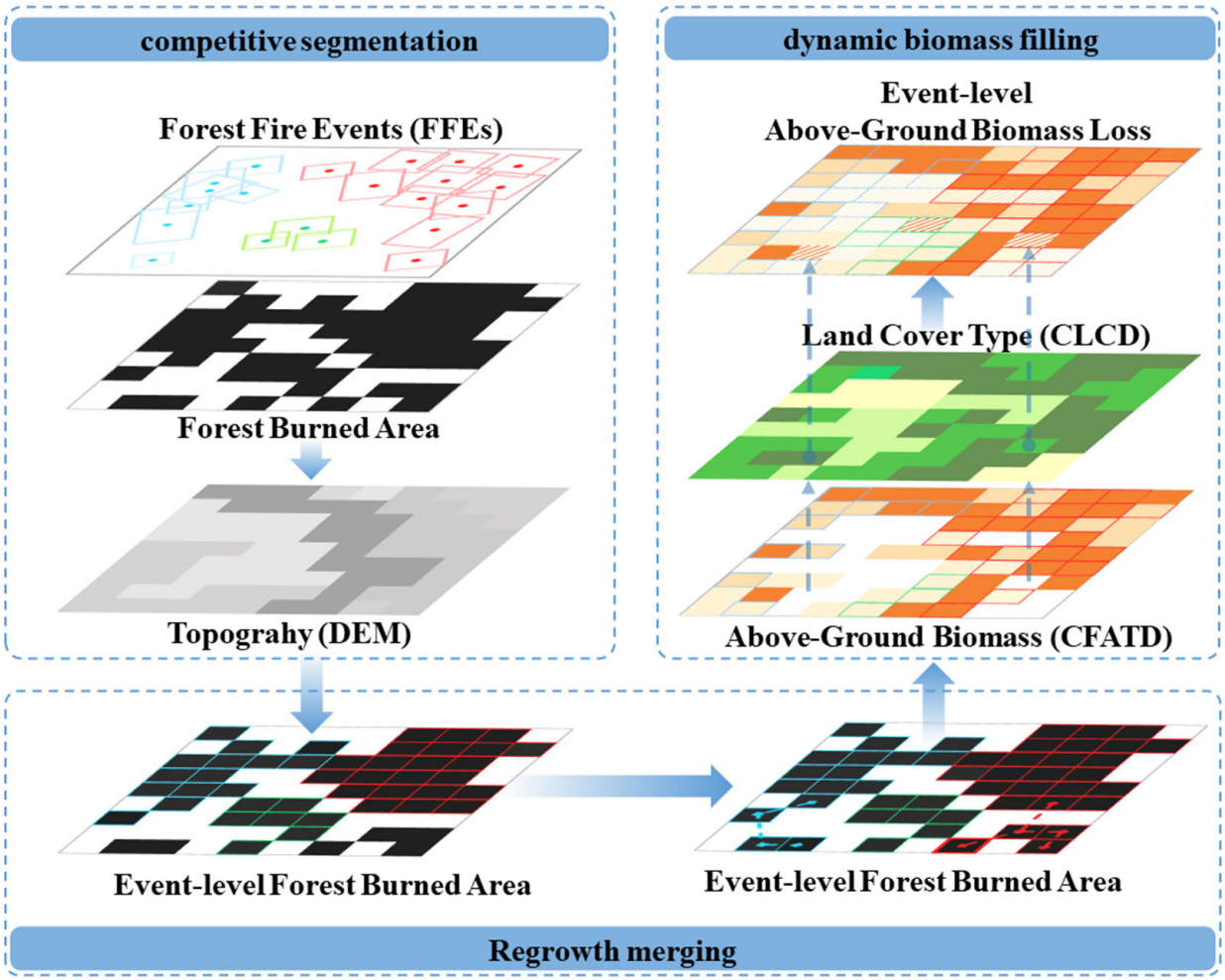


Figure 5. Schematic diagram of the morphological reconstruction algorithm. The colors, arrows, frames, and patterns are used schematically to distinguish different data layers, event-level segments, processing steps, and information transfer, rather than to represent fixed quantitative values.

(1) Competitive segmentation of potential energy fields: Targeting the spatial adhesion of adjacent FFEs, a Constrained Watershed Transformation was introduced. Using the clustered AFS groups as seeds S, and the BA as a mask M, a fire spread potential energy field based on geodesic distance $D_{\text{geo}}(x, S)$ and topographic gradient $\nabla Z(x)$ was constructed:

$$P(x) = \alpha \cdot D_{\text{geo}}(x, S) + \beta \cdot \nabla Z(x),\ x \in M \quad (1)$$

where is the pixel to be classified, and, are the weight coefficients. By simulating the diffusion of potential energy, the algorithm successfully achieved the topological decoupling of spatially adjacent yet physically independent fire units.

(2) Morphological regrowth and merging: To repair BA data fragmentation caused by cloud and smoke obscuration, the algorithm iteratively captured isolated BA within a 600 m neighborhood of the segmentation boundaries. Simultaneously, fragments with an area <0.3 ha within 600 m of the main fire perimeter were treated as spotting and topologically fused, thereby ensuring the morphological integrity of the FFEs.

(3) Dynamic AGB filling: Addressing the issue of AGB data absence in certain burned areas (such as agro-forestry ecotones) due to atypical forest lands, a CLCD-AGB empirical mapping matrix was constructed:

$$LUT(c) = \begin{cases} 5.0, & c = 1(Cropland), \\ 120.0, & c = 2(Forest), \\ 25.0, & c = 3(Shrub), \\ 8.0, & c = 4(Grassland), \\ 0.0, & c = 5(Water), \\ 0.0, & c = 6(Snow/Ice), \\ 1.0, & c = 7(Barren), \\ 0.0, & c = 8(Impervious), \\ 15.0, & c = 9(Wetland). \end{cases} \left(Mgha^{-1}\right) \quad (2)$$

$$AGB_{fill}(p) = \begin{cases} AGB_{raw}(p), & \text{if } AGB_{raw}(p) > 0, \\ LUT(L_{CLCD}(p)), & \text{if } AGB_{raw}(p) = 0. \end{cases} \quad (3)$$

where p represents the pixel location; $AGB_{raw}(p)$ is the original AGB observation value; $AGB_{fill}(p)$ is the filled AGB value; and $LUT(\cdot)$ is the empirical AGB look-up table based on a priori knowledge. Accordingly, $LUT(L_{CLCD}(p))$ denotes the empirical AGB value assigned according to the CLCD land-cover class. This step effectively restored the actual AGB baseline in complex habitats such as agroforestry ecotones.

2.4. Algorithm Validation

The main strength of the event-level forest fire reconstruction framework developed in this study is that it reduces redundancy in multi-source remote sensing observations by organizing them into spatiotemporally coherent FFEs. To address active-fire pixel overlap and background thermal noise from the joint observations of MODIS and dual-satellite VIIRS, the MST-DBSCAN framework was used to group detections in space and time within a common observation framework. Starting from 497,834 raw AFSs detected during 2012–2024, the framework removed unusable detections, aggregated the retained observations through MST-DBSCAN, and finally reconstructed 41,215 validated FFEs with independent life cycles, corresponding to an AFS assimilation rate of 90.4% (Appendix Table A1; Figure S1). This event-level reconstruction reduced the redundancy associated with repeated satellite observations and provided a more consistent basis for subsequent analyses of FFE duration, BA, and CFRP.

Based on the reconstructed fire records, we further integrated discrete instantaneous FRP observations from multiple sensors into fire-level CFRP. To enhance the physical plausibility of the reconstructed fire conditions and mitigate the impact of outlier detection, we implemented a rigorous outlier filtering process, which includes removing isolated noise points under extreme burned area conditions (e.g., MinPts = 1 and BA > 100 ha) and applying a 99th percentile cutoff to both CFRP and AGB. Additionally, the 2024 AGB values were approximated using the 2023 baseline dataset. Combined with spatial filtering, these steps reduce artificial fragmentation introduced by satellite pass discontinuities and limit the inflation of fire counts caused by repeated multi-satellite observations.

To further assess whether this filtering process retained only detections spatially consistent with GABAM rather than prioritizing physically plausible fire events, we conducted independent manual interpretations based on Sentinel-2 imagery for the samples retained and excluded at both the AFS and FFE levels. Across the entire study area, 332 out of 400 sampled cases (83.0%) could be classified with reasonable confidence using pre- and post-event Sentinel-2 imagery, while the remaining 68 cases (17.0%) were classified as uncertain, due to limitations in optical evidence caused by cloud cover, dense smoke, canopy shading, low fire intensity, short duration, or the lack of sufficiently clear post-fire traces. At the AFS level, the retained group included 92 true fire points, 13 non-fire points, and

15 uncertain samples, while the excluded group included 20 true fire points, 74 non-fire points, and 26 uncertain samples. At the FFE level, the corresponding counts for the retained group were 58, 7, and 15, while those for the discarded group were 8, 60, and 12.

Taken together, these results indicate that the filtering procedure did not merely retain detections matching burn scars. Rather, it significantly improved the physical credibility of the retained records, while still carrying a limited but non-negligible risk of omission for fires with faint traces or those that are optically difficult to distinguish. This reinforces confidence that the extreme high-energy fires analyzed in this study primarily reflect actual fire processes, rather than artifacts resulting from repeated observations, background thermal noise, or overly stringent burn-scar screening.

As an additional line of evidence, the physical closed-loop validation phase examined the original satellite confidence structure of the retained and eliminated pixel groups after morphological reconstruction based on high-resolution optical burn scars [24,25]. The results show a clear enrichment of higher-quality observations in retained pixels successfully matched with authentic physical BA: the cumulative proportions of medium-to-high confidence (Nominal and High) pixels for MODIS and VIIRS remained high at 95.8% and 92.4%, respectively. By contrast, the internal quality structure of eliminated scarless artifact pixels without actual burning, such as misidentified high-temperature smoke plumes or highly reflective backgrounds, declined substantially. The proportion of High-confidence pixels for MODIS and VIIRS decreased from 19.5% and 3.3% in the retained group to only 11.3% and 1.8% in the eliminated group, respectively. This contrast provides further support for the effectiveness of the optical–thermal cross-check in accommodating confidence differences among sensors and in removing false-positive signals that are common in single-source remote sensing [17,21,26]. At the same time, the independent Sentinel-2 validation indicates that the remaining omission risk is mainly concentrated in a limited subset of weak, short-lived, or heavily obscured fires, rather than reflecting a general tendency of the framework to remove true FFEs.

To further summarize the heterogeneity of reconstructed FFEs, we defined nine fire typologies using an attribute-based rule classification framework applied to event-level attributes. The classification combined land-cover context, topographic position, burning duration, BA, CFRP, and AGB-related indicators derived from the reconstructed event database. Events were first assigned to broad environmental settings, including forest interior, agroforestry ecotone, cropland interior, WUI, topographic–alpine terrain, and other marginal landforms, and were then further separated according to persistence, spread scale, CFRP, AGB level, and slope/elevation conditions. The resulting labels were subsequently evaluated in multidimensional feature space, where principal component analysis (PCA) was used to visualize class distribution and Random Forest with stratified cross-validation was used to assess class separability and reproducibility. In this evaluation step, PCA and Random Forest were used only to assess the predefined rule-based labels rather than to generate them. The final validation yielded a Macro-F1 of 0.9935 and a Weighted-F1 of 0.9964, while the first two principal components explained 42.65% of the total variance. These results indicate that this typology framework retains a clear multidimensional structure in independent validation but also exhibits a high degree of reproducibility.

3. Results

3.1. Temporal Characteristics

3.1.1. Interannual Characteristics

The analysis is based on clustered events (Process level), i.e., events identified after spatiotemporal clustering but prior to final validation. Interannual variations in event frequency and CFRP show contrasting behaviors over 2012–2024 (Figure 6). Before 2018,

fire activity exhibited moderate interannual variability, with a pronounced peak in both frequency and CFRP in 2014, followed by a decline toward 2017. After the inclusion of NOAA-20 in 2018, the number of detected events increased markedly relative to the legacy dual-source baseline (MODIS and Suomi NPP), with particularly high frequencies observed in 2022 and 2023. However, CFRP does not follow this pattern: while 2023 represents a clear high-CFRP year, 2022 exhibits relatively low CFRP despite elevated event counts. Overall, the CFRP series maintains comparable magnitudes and temporal trajectories between the dual-source baseline and the full three-sensor dataset, indicating that the post-2018 increase in event frequency is not accompanied by a proportional increase in total CFRP [21,26].

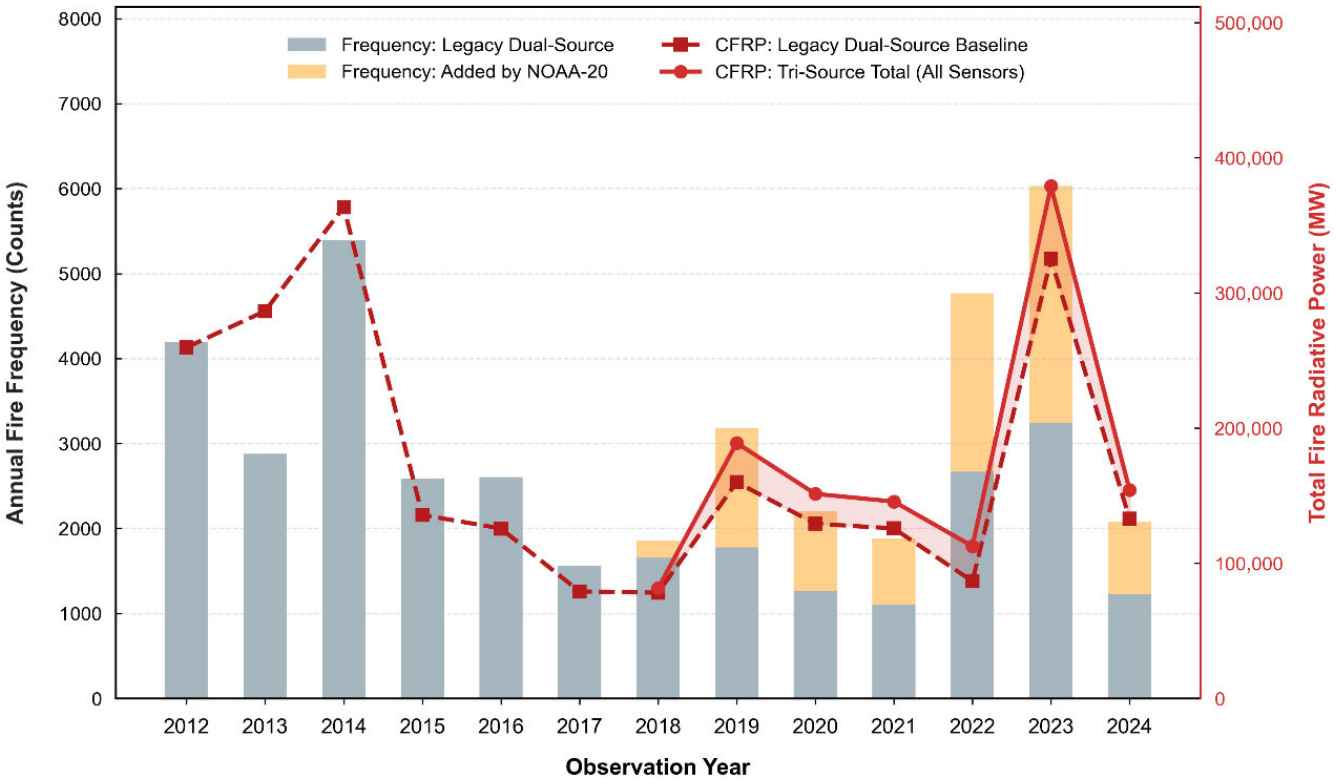


Figure 6. Total annual frequency of FFEs and CFRP.

Decomposition of source contributions (Figure 7) shows that this divergence is structurally controlled by sensor composition. The expansion in detected events after 2018 is dominated by single-sensor detections, whereas high-CFRP events remain concentrated in multi-sensor observations. In particular, NOAA-20-only events account for a substantial fraction of event frequency but contribute only a limited share of total CFRP, while NOAA-20-involved events contribute the majority of total CFRP. This indicates that the apparent increase in annual fire frequency is primarily associated with the enhanced detection of low-intensity events, whereas interannual variability in total CFRP is governed by a limited number of high-energy fires. This asymmetric relationship between event frequency and energy contribution provides direct evidence of frequency–impact decoupling at the interannual scale. In some years, increases in event counts mainly reflect the accumulation of low-intensity fires, whereas interannual peaks in total CFRP are controlled by a limited number of high-CFRP events. Annual fire activity in the study area therefore cannot be interpreted from event counts alone.

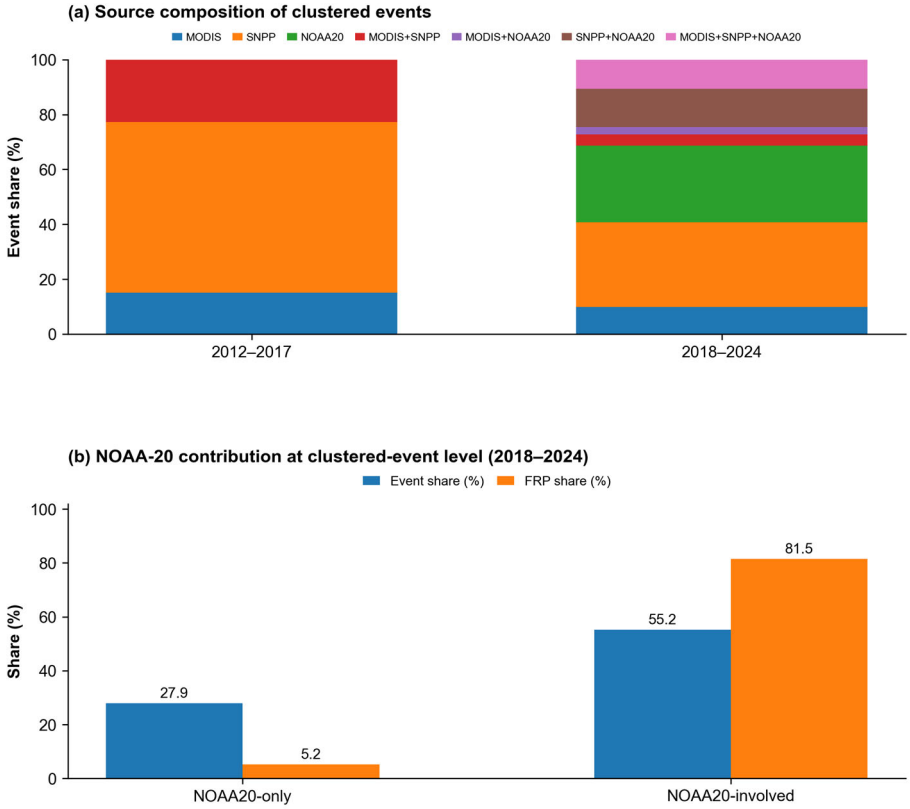


Figure 7. Source composition and NOAA-20 contribution at the clustered-event (Process) level. (**a**) Event-share distribution of different sensor combinations for 2012–2017 and 2018–2024. (**b**) Comparison of event share and CFRP share for NOAA-20-only events and NOAA-20-involved events during 2018–2024. All statistics are derived from clustered events after spatiotemporal clustering but prior to final validation. The figure quantifies the contribution of newly detected events following the inclusion of NOAA-20 and illustrates the asymmetric relationship between event frequency and total CFRP.

3.1.2. Seasonal/Phenological Characteristics

The interannual–solar-term heatmap (Figure 8) shows a strong seasonal concentration of forest fire activity in Yunnan. The principal peak occurred during the late dry season, from the "Awakening of Insects" to the "Clear and Bright" solar terms, before the onset of the Southwest Monsoon [20]. Within this interval, which accounts for approximately one-quarter of the year, 32.8% of all reconstructed FFEs during 2012–2024 were recorded. After the "Start of Summer" solar term, fire occurrence declined sharply, with heatmap frequencies decreasing by as much as 78.7%. Thus, at the provincial scale, reconstructed fire activity was concentrated within a relatively narrow late dry-season window rather than being evenly distributed across the year.

Interannual comparison shows that this seasonal concentration remained broadly stable even in high-fire years [13]. In 2014, 2021, and 2023, fire occurrence increased substantially within the spring peak period, with spring event counts reaching up to 2.0 times the 13-year average. However, the boundaries of the main seasonal peak did not show substantial extension beyond the usual late dry-season period. This means that interannual variation was expressed mainly as an intensification of fire activity within the established spring concentration window rather than as a major shift in the seasonal timing of the fire season. In other words, years with elevated fire activity were characterized more by denser concentration within the main peak than by an obvious expansion of that peak into adjacent seasonal periods.

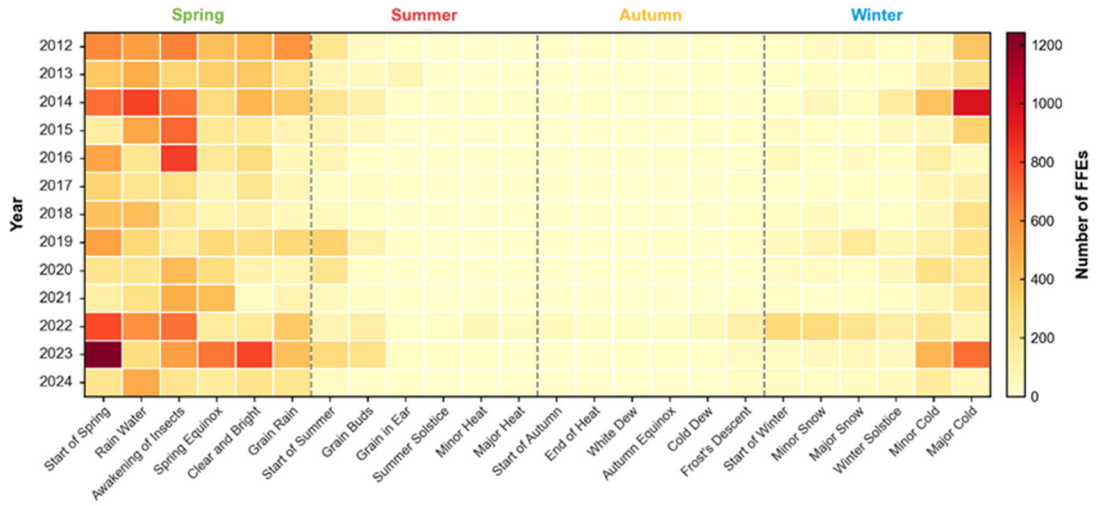


Figure 8. Seasonal distribution of FFEs and CFRP.

3.1.3. Diurnal Characteristics

The diurnal distribution of fire activity (Figure 9) shows that daytime events dominated the reconstructed event database. Across the full study period, 82.8% of all FFEs occurred during the daytime, and both the median CFRP and the upper range of CFRP values were generally higher during the day than at night. Thus, daytime burning accounted for most of the total event frequency and most of the central tendency of event-level CFRP in Yunnan.

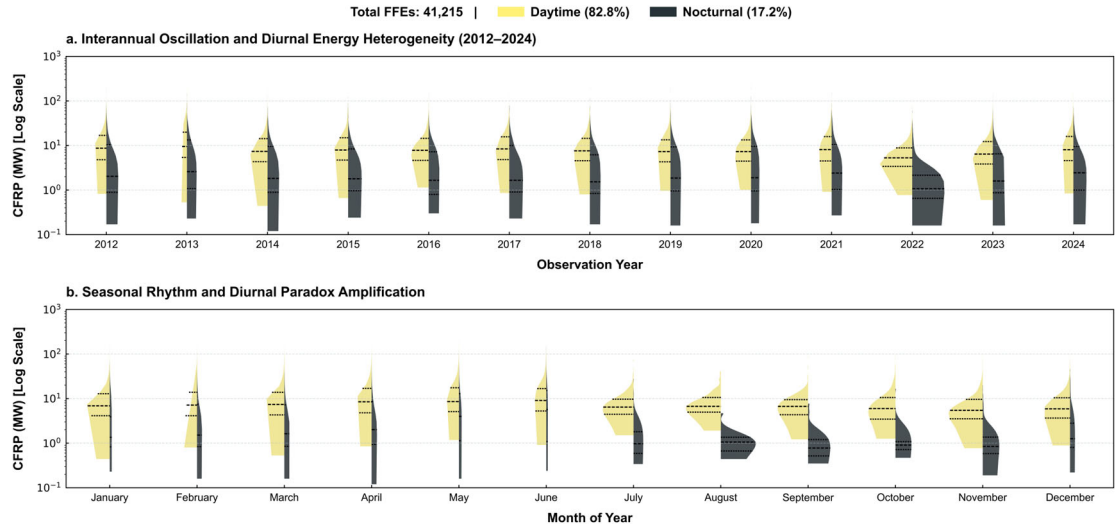


Figure 9. Diurnal distribution of CFRP. (**a**) Interannual Oscillation & Diurnal Power Heterogeneity (2012–2024). (**b**) Seasonal Rhythm & Diurnal Paradox Amplification.

At the interannual scale, however, nighttime activity varied markedly among years [27,28]. In 2022, nocturnal fires accounted for 12.8% of all reconstructed events, and the nocturnal median CFRP was 1.07 MW. In 2023, nocturnal activity increased to 1250 events, corresponding to 20.7% of all events, and the nocturnal median CFRP increased to 1.60 MW. Similar expansion of the upper tail of nocturnal CFRP was also visible in other high-fire years, including 2014 and 2021. These results indicate that interannual variability affected not only the total number of events, but also the relative contribution and energy distribution of nighttime fires. The comparison between 2022 and 2023 is especially notable because both years had high event counts, yet the nocturnal share and nocturnal median CFRP were clearly higher in 2023.

At the seasonal scale, nocturnal fire activity strengthened progressively from the early dry season toward the end of the spring fire season [27,28]. In January, nocturnal fires represented 6.7% of monthly events, with a median CFRP of 1.36 MW. This proportion increased to 27.6% in April and 30.1% in May. The seasonal increase in nocturnal activity was accompanied by an upward shift in the energy distribution of nighttime fires. In May, the nocturnal median CFRP reached 4.00 MW, and the logarithmic violin plots show that the upper tail of nocturnal CFRP extended into the >100 MW range during the January–June dry-season window. Taken together, these results indicate that nighttime burning became both more frequent and more energetic from late winter to late spring.

Figure 9 also suggests that the daytime–nighttime contrast was not constant throughout the year. During the early dry season, nocturnal activity remained limited in both frequency and median power, whereas toward the end of the spring fire season the nocturnal distribution broadened substantially and overlapped more strongly with the daytime high-power range. Therefore, the diurnal signal in the reconstructed dataset is best described not as a fixed day–night contrast, but as a pattern that varies across years and becomes seasonally more pronounced as the dry season progresses.

3.1.4. Combustion Persistence Characteristics

Combustion persistence in the study area was evaluated using period-specific operational thresholds rather than a single fixed duration criterion (Figure 10). These thresholds were derived from the minimum cross-sensor detection interval for the same FFE plus a 15 min redundancy allowance, corresponding to 105 min for 2012–2017 and 75 min for 2018–2024. Because the persistence threshold differed between the two observation periods, threshold-based persistence proportions are most appropriately interpreted within each period, whereas pooled summaries across 2012–2024 should be treated as descriptive references rather than directly comparable fire-behavior fractions. Across the full dataset, 16,674 events (40.46%) were extinguished within the corresponding period-specific threshold, whereas 24,541 events (59.54%) persisted beyond it. However, this pooled proportion mainly reflects the coexistence of two different threshold settings rather than a temporally uniform persistence regime.

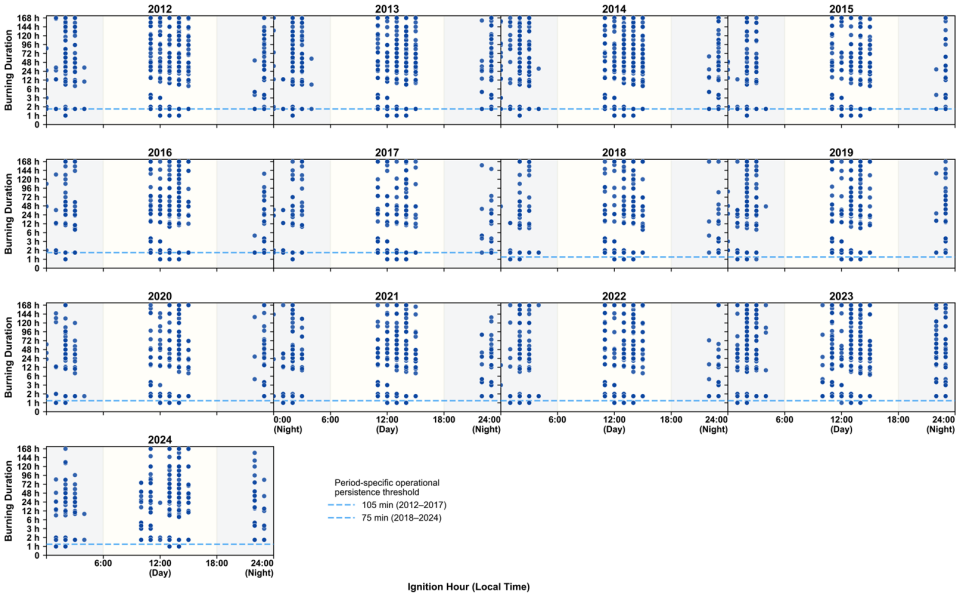


Figure 10. Annual relationship between ignition time and burning duration of FFE. The dashed horizontal line indicates the period-specific operational persistence threshold, defined according to the minimum cross-sensor detection interval for the same FFE plus a 15 min redundancy allowance, corresponding to 105 min for 2012–2017 and 75 min for 2018–2024.

Under the 2012–2017 threshold setting (105 min), short-lived combustion remained dominant. In this period, 13,979 events (72.74%) were extinguished within 105 min, whereas 5238 events (27.26%) persisted beyond the threshold. The CFRP contrast between the two groups was substantial: events at or below the threshold had a mean CFRP of 23.24 MW, whereas events persisting beyond 105 min reached 176.71 MW, corresponding to a difference of approximately 7.6 times. Additional annual CFRP-contribution analysis further shows that these threshold-exceeding events, although accounting for only 27.26% of all events, contributed 74.02% of the total CFRP in this period (Figure S2). Thus, under the earlier observation configuration, the 105 min threshold effectively separated a dominant short-duration group from a much smaller but energetically dominant persistent subset (Figure 11 and Figure S2).

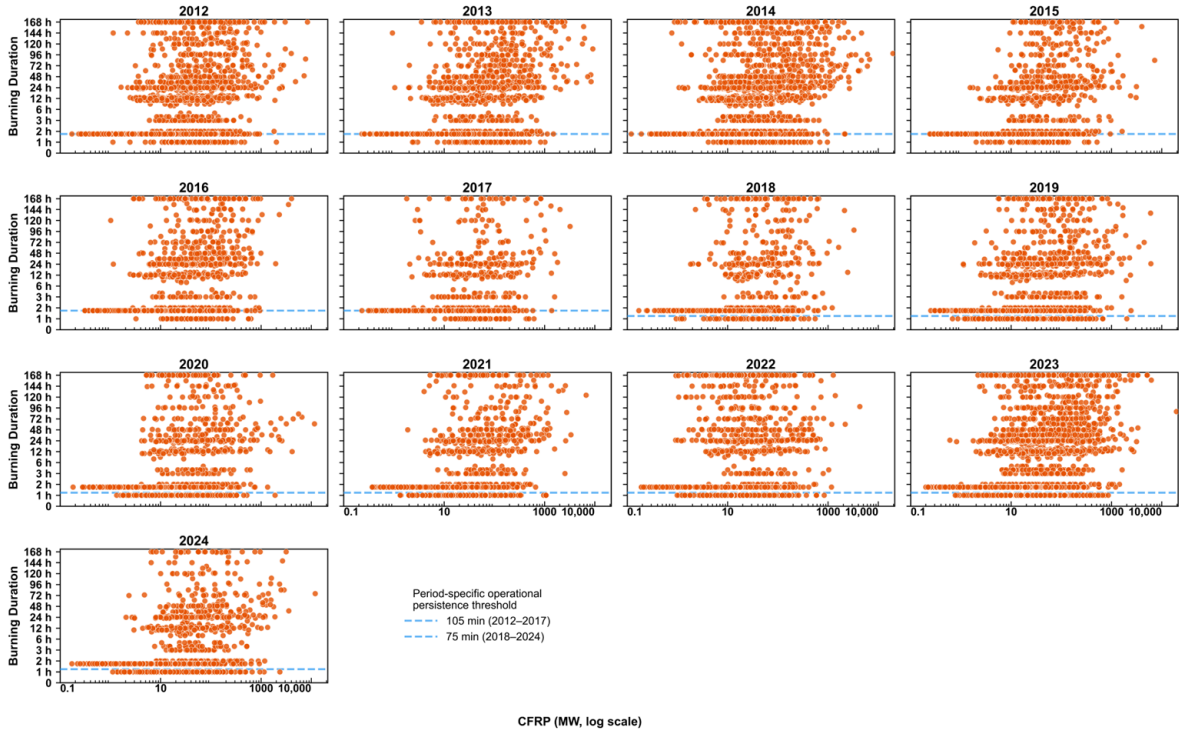


Figure 11. Annual relationship between CFRP and burning duration of FFEs. Together, the two panels illustrate the temporal distribution of ignition timing, combustion duration, and power release under the period-specific persistence framework adopted in this study.

Under the 2018–2024 threshold setting (75 min), the structure changed markedly. In this period, only 2695 events (12.25%) remained within the threshold, whereas 19,303 events (87.75%) persisted beyond it. However, the contrast in mean CFRP between the two threshold classes was much weaker than in 2012–2017, with values of 51.29 MW for events within the threshold and 55.71 MW for events beyond it. Consistently, the threshold-exceeding group contributed 88.61% of total CFRP, which was close to its event share (87.75%). This indicates that the reduced threshold captured a broader range of post-ignition persistence states and functioned mainly as an observation-adjusted separator between shorter and longer combustion phases, rather than as a sharp divider between low-power and high-CFRP events. Accordingly, persistence statistics after 2018 are best interpreted in relation to the revised observation framework rather than as directly equivalent to the 2012–2017 threshold classes (Figure 11 and Figure S2).

The additional standardized persistence analysis supports this interpretation (Figure S3). When duration was normalized by the period-specific threshold, the median persistence ratio was 1.0 in 2012–2017 and 1.4 in 2018–2024, while the upper-tail structure remained

pronounced in both periods, with P90 values of 23.77 and 28.00, respectively. This result indicates that long-duration events persisted well beyond the operational thresholds in both periods, but that the change in threshold definition also altered how much of the duration distribution was classified as "persistent". In other words, the threshold adjustment did not eliminate the long-tail structure of fire duration, but it did modify the boundary between short-lived and threshold-exceeding events (Figure S3).

A clear diurnal asymmetry was evident in the earlier period but weakened after 2018 (Figure S4) [27]. In 2012–2017, nighttime ignitions were substantially more likely than daytime ignitions to exceed the 105 min threshold: the exceedance rate was 40.88% at night compared with 24.40% during the day, corresponding to an odds ratio of 2.14 and a risk ratio of 1.68. By contrast, in 2018–2024, exceedance rates were similarly high for both nighttime (85.98%) and daytime (88.11%) ignitions, with an odds ratio of 0.83 and a risk ratio of 0.98. This suggests that the nocturnal persistence advantage was clearly expressed under the 105 min threshold setting, but became much less distinct once the operational threshold was reduced to 75 min [28]. At the same time, marked interannual variability remained evident. Under the 105 min threshold, the highest persistent-event proportions occurred in 2013 (30.83%), 2012 (29.68%), and 2014 (26.21%), whereas 2017 showed the lowest value (22.98%) within that period. Under the 75 min threshold, persistent-event proportions were consistently high, reaching 94.47% in 2018, 92.05% in 2022, 87.57% in 2024, and 87.20% in 2023, with the lowest value in this period recorded in 2019 (83.02%). Annual mean duration and annual mean CFRP did not vary synchronously: for example, 2022 had the highest mean duration (111.14 h) but a relatively low mean CFRP (23.63 MW), whereas 2013, 2021, and 2024 showed comparatively high mean CFRP values (99.52 MW, 77.40 MW, and 74.34 MW, respectively). Taken together, these results indicate that combustion persistence in Yunnan was highly heterogeneous across both years and observation periods, and that the relationship between FFE duration and CFRP depended not only on event longevity itself but also on the operational persistence threshold associated with the underlying satellite observation framework (Figure 10 and Figure S4).

3.1.5. Fuel Load Characteristics

Figure 12 summarizes the affected AGB characteristics of reconstructed FFEs across interannual, seasonal, and event-duration dimensions. At the interannual scale, the mean AGB density within event perimeters varied relatively moderately among years, whereas the average AGB affected per event changed much more strongly. During 2014, 2016, and 2023, the average affected AGB per FFE reached approximately 3000–4000 tons, which was about 4–5 times higher than in lower-impact years. This contrast indicates that years with greater event-level AGB impact were distinguished less by abrupt shifts in AGB density per unit area and more by the larger AGB totals involved within individual fire-event perimeters. In addition, Figure 12c shows a significant logarithmic relationship between burned area and affected AGB, indicating that larger events tended to involve substantially greater AGB consumption.

At the seasonal scale, median affected AGB reached its annual maximum in February and March. A secondary peak was also present in October, when median affected AGB reached 408 tons, followed by a decline in November. Thus, the seasonal AGB pattern was characterized by a main late-winter to early-spring maximum and a smaller autumn peak. This means that the annual cycle of affected AGB was not strictly unimodal. Instead, most of the year's largest median AGB losses were concentrated in the late dry season, but a smaller second pulse was also present in autumn.

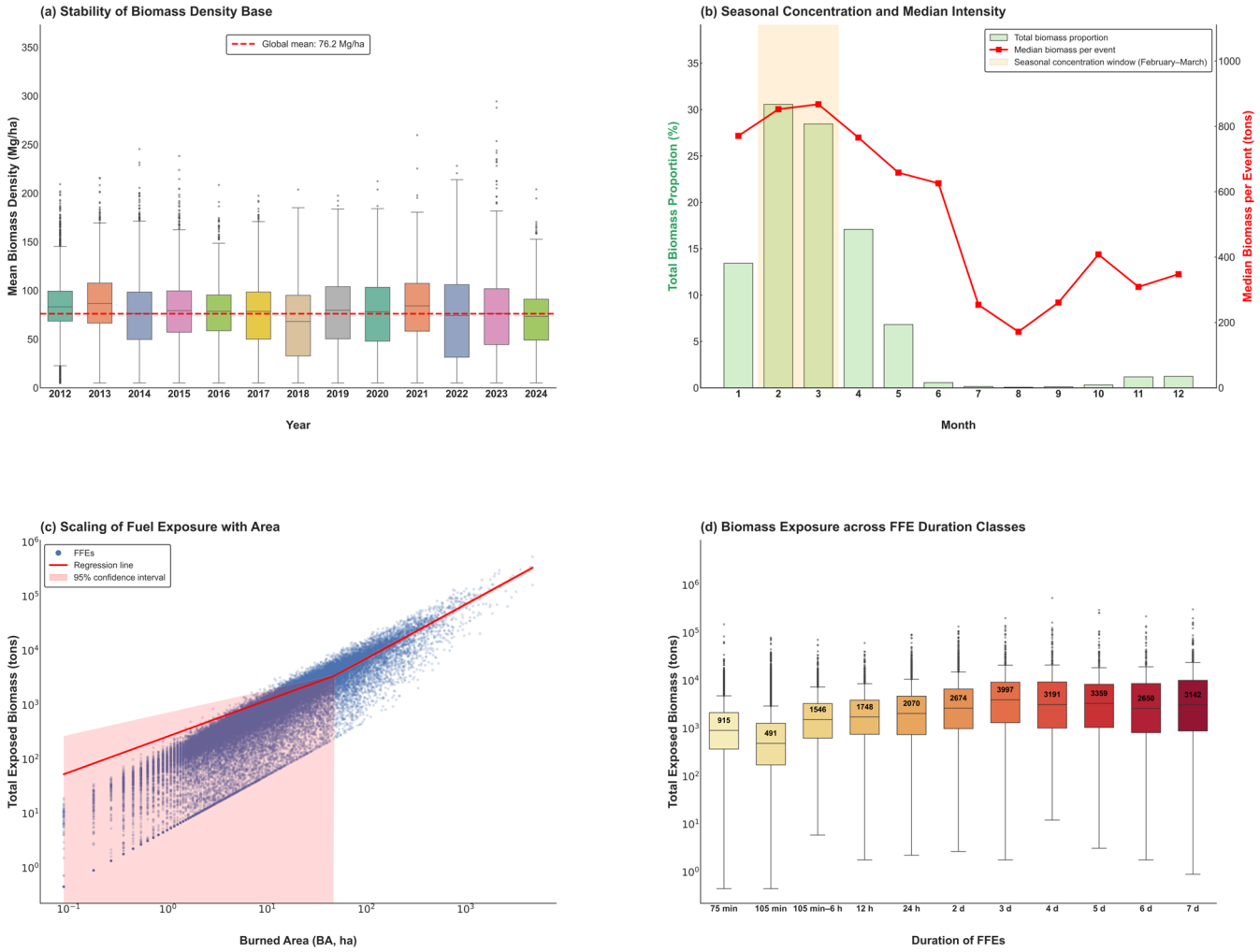


Figure 12. The spatiotemporal distribution of fuel load in FFEs.

Event duration was also strongly associated with AGB consumption. In the shortest duration class shown in Figure 12d, the median affected AGB was about 600 tons. After 1–2 days, the median affected AGB increased to about 2400 tons, and by day 7 it approached 4000 tons. These values indicate a clear non-linear increase in affected AGB with longer event duration. The curve is not a simple linear step-by-step rise; rather, the largest increase occurs after events extend beyond the shortest duration class and persist into multi-day burning. Thus, extended event duration was associated with a substantial enlargement of AGB impacts at the event level.

The event-level summaries further indicate that fires surviving into the nighttime period were, on average, located at higher elevations than daytime events. In combination with the duration–AGB relationship, this pattern suggests that larger affected AGB was associated not only with larger burned perimeters, but also with longer-lasting events that extended across multiple observation intervals and, in many cases, into the nighttime period, consistent with the broader importance of nocturnal fire persistence [27,28]. Therefore, the AGB results provide a useful bridge between burned-area expansion, event persistence, and the physical magnitude of fire impact.

3.2. Spatial Characteristics

3.2.1. Characteristics of the Study Area

The spatial distribution of reconstructed FFEs showed marked regional heterogeneity across Yunnan (Figure 13; Table 3) [12]. Southeast Yunnan recorded 21,129 events,

accounting for 51.3% of all reconstructed events, followed by Southwest Yunnan with 10,587 events (25.7%). Together, these two southern regions contributed 77.0% of all events and 58.98% of total CFRP. However, their mean CFRP per event remained comparatively low, at 44.6 MW in Southeast Yunnan and 48.0 MW in Southwest Yunnan. Thus, the south of the province concentrated most reconstructed events, but not the highest mean CFRP per event.

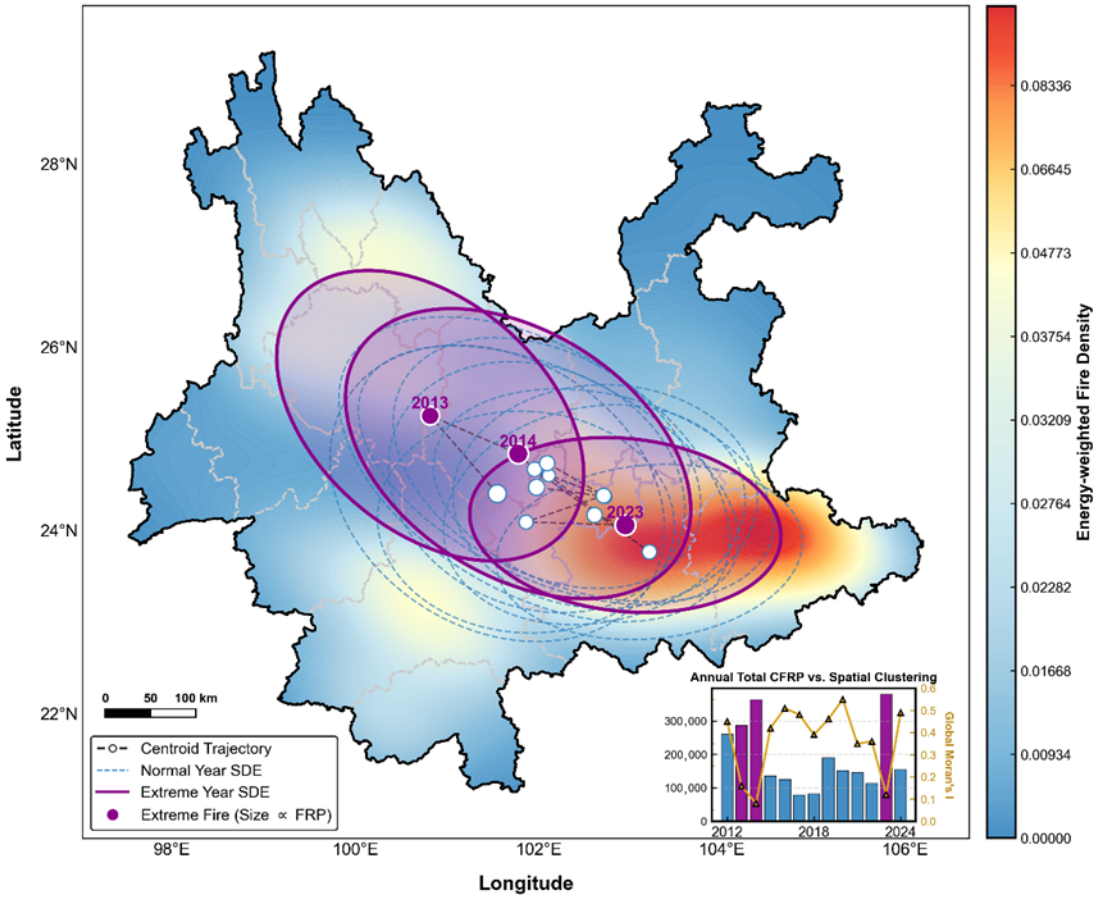


Figure 13. Distribution of CFRP in the study area (2012–2024). In the inset panel, the bars show the annual total CFRP, with blue bars representing normal years and purple bars representing extreme fire years. The brown line with triangle markers represents the annual Global Moran's I, corresponding to the right y-axis and indicating the degree of spatial clustering.

Table 3. Statistics of FFEs and CFRP in the Five Major Regions of the study area (2012–2024).

Geographic_Region	FFEs_Count	Total_CFRP	Mean_CFRP	FFEs_Count_ Percent (%)	CFRP_ Percent (%)
Southeast Yunnan	21,129	944,053.3	44.6	51.3	38.33
Southwest Yunnan	10,587	508,743.4	48.0	25.7	20.65
Northwest Yunnan	4132	555,586.3	134.4	10.03	22.56
Central Yunnan	3304	356,459.7	107.8	8.02	14.47
Northeast Yunnan	2035	98,407.8	48.3	4.94	4

By contrast, Northwest and Central Yunnan contributed much smaller shares of total events but substantially larger shares of CFRP relative to their event counts. Northwest Yunnan recorded 4132 events (10.03%) and contributed 22.56% of total CFRP, with a mean CFRP of 134.4 MW per event. Central Yunnan recorded 3304 events (8.02%) and contributed 14.47% of total CFRP, with a mean CFRP of 107.8 MW per event. The mean CFRP per

event in these two regions was therefore about 2.4–3.0 times higher than in Southeast and Southwest Yunnan. These results indicate that the regional distribution of event frequency was not proportional to the regional distribution of mean event-level CFRP.

Northeast Yunnan had the lowest values in both event frequency and total CFRP, with 2035 events (4.94%), 4.00% of total CFRP, and a mean CFRP of 48.3 MW per event. Relative to the province-wide spatial pattern, Northeast Yunnan therefore occupied the lower end of both occurrence frequency and total CFRP contribution. In this sense, the five-region comparison was not simply a gradient from south to north, but a differentiated structure in which the south dominated event numbers, the central–northwestern regions showed the highest per-event power, and the northeast remained low on both dimensions [20,29].

Figure 13 further shows that the spatial concentration of event occurrence and the spatial concentration of total CFRP were not identical across the province. Regions with dense event occurrence did not necessarily coincide with regions of highest per-event CFRP intensity. Therefore, the regional statistics indicate that the spatial pattern of fire activity in Yunnan should be described using at least two complementary dimensions: occurrence frequency and event-level CFRP intensity. Taken together, Table 3 and Figure 13 show that southern Yunnan was the main zone of high event concentration, whereas Northwest and Central Yunnan contributed a disproportionate share of high-intensity events.

3.2.2. Topographical Characteristics

Topography influenced the spatial organization of fire activity, but its effects were expressed more clearly in slope-related power concentration and diurnal elevational separation than in a simple drought-driven upslope shift (Figure 14). As shown in Figure 14a, AGB-weighted power allocation (BWEA) was concentrated mainly on gentle-to-moderate slopes under the four cardinal aspects. The five highest aspect–slope combinations were E/5–10° (12.84% of total BWEA), N/5–10° (10.24%), S/10–15° (9.94%), E/10–15° (9.81%), and W/10–15° (9.71%). Together, these five combinations accounted for 52.54% of total BWEA, indicating that fire-energy release was concentrated within a limited set of topographic settings rather than evenly distributed across the terrain.

The slope-stratified summaries further show that this concentration was largely confined to the 5–15° range. The 5–10° and 10–15° classes contained the largest numbers of events and the highest BWEA totals, whereas steeper slopes contributed much less to total fire energy despite their generally higher mean AGB values. In Figure 14a, slope classes above 30° were grouped for visualization because their BWEA contributions were relatively small at the plotting scale; this graphical simplification did not alter the event-level BWEA calculation. The supplementary terrain-share and selectivity analyses further indicate that several gentle-to-moderate slope combinations under the cardinal aspects were enriched relative to their background terrain proportion. In other words, the concentration of fire energy in these settings cannot be explained solely by terrain availability, but indicates a non-random topographic concentration of fire-energy release [29].

The elevational distribution of AGB-weighted fire activity showed a different pattern. In Figure 14b, the AGB-weighted elevation centroid was 1928.6 m in extreme drought years and 1965.0 m in normal years, corresponding to a difference of −36.4 m. However, the 95% confidence intervals overlapped substantially, and the permutation test indicated that this difference was not statistically significant (p = 0.425). Therefore, the vertical center of fire energy release remained broadly similar between extreme and normal years and did not provide evidence for a statistically supported upward shift under extreme drought conditions.

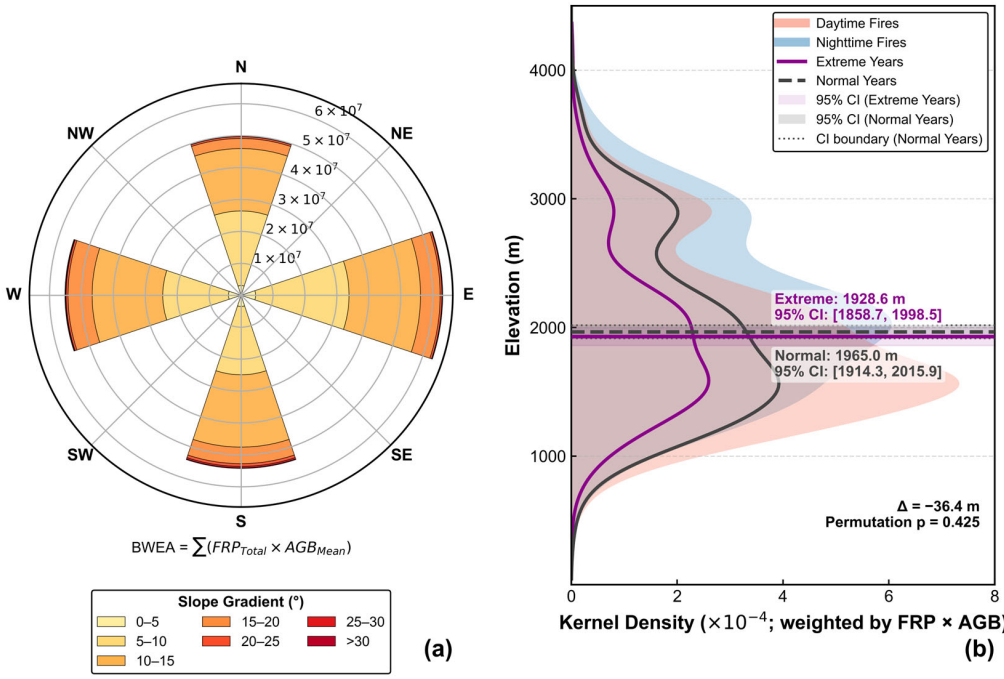


Figure 14. Topographic modulation of AGB-weighted fire-energy allocation in Yunnan Province during 2012–2024. (**a**) AGB-weighted power allocation (BWEA) across aspect–slope combinations, highlighting the concentration of fire-energy release on gentle-to-moderate slopes under major aspect directions. (**b**) Elevational distribution of AGB-weighted fire activity for daytime and nighttime FFEs, and for extreme drought years and normal years.

By contrast, the day–night contrast in elevation was larger and statistically robust. The AGB-weighted elevation centroid of nighttime fires was 215.03 m higher than that of daytime fires, and this difference was significant (permutation p = 0.0002). The density curves in Figure 14b are consistent with this result, showing that nighttime fire activity was more concentrated at relatively higher elevations than daytime fire activity. The nighttime density curve also shows a secondary high-elevation concentration around 2800–3000 m, which is consistent with the elevational separation between daytime and nighttime fire activity but should be interpreted as a distributional feature rather than as an independent elevation threshold. The additional slope-by-day/night summaries further indicate that this diurnal separation was most evident on gentle-to-moderate slopes, where nighttime fires tended to occur at higher elevations and, in several slope classes, were also associated with higher mean CFRP than daytime fires. Taken together, these results indicate that the dominant topographic signal in the study area was not an interannual upward redistribution of fire activity under drought, but a structured concentration of fire energy in limited slope–aspect combinations and a clear day–night separation along the elevational gradient.

3.2.3. Characteristics of FFEs

Traditional fire risk assessments often emphasize occurrence frequency, but the reconstructed event-level database indicates that the ecological consequences of FFEs in Yunnan were highly heterogeneous across fire types [30,31]. To summarize this heterogeneity, the reconstructed FFEs were grouped into nine fire typologies using the rule-based classification framework described above. The resulting labels were evaluated in multidimensional feature space, where Random Forest validation with stratified cross-validation showed very high class separability, with a Macro-F1 of 0.9935 and a Weighted-F1 of 0.9964 [32,33]. By contrast, the first two principal components explained 42.65% of the total variance,

indicating that the typologies retained substantial multidimensional structure beyond a two-dimensional projection. Accordingly, Figure 15a should be interpreted primarily as a low-dimensional visualization of category structure, whereas the Random Forest results provide the main evidence for classification reproducibility and separability. Overall, the typology system reveals a clear mismatch between the share of event frequency and the share of physical fire impact represented by burned area, CFRP, and AGB loss [30].

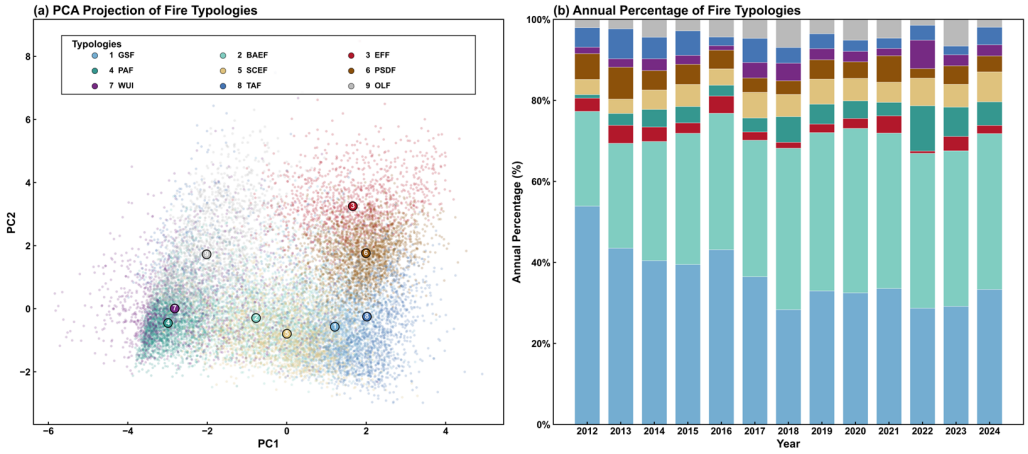


Figure 15. Multidimensional distribution and annual proportions of the nine fire typologies in Yunnan Province during 2012–2024. (**a**) PCA projection of the nine predefined rule-based fire typologies in multidimensional feature space. The first two principal components explained 42.65% of the total variance. (**b**) Annual percentage distribution of the nine fire typologies. The colored segments in the stacked bars use the same color scheme as the typology legend in panel (**a**), with each color representing one fire typology. Random Forest validation with stratified 5-fold cross-validation yielded a Macro-F1 of 0.9935 and a Weighted-F1 of 0.9964. Table 4 summarizes the event counts, proportions, and dominant habitat/spatial niche characteristics of each typology.

Table 4. Characteristics of the nine fire typologies during 2012–2024.

Fire Typology	Total Events	Proportion	Dominant Habitat/ Spatial Niche
General Sporadic Forest Fires	15,154	36.77%	Contiguous closed-canopy forests/Secondary forest background matrix
Basin Agroforestry Ecotone Escaped Fires	14,089	34.18%	Basin edges and gentle slope agroforestry ecotones
Explosive Forest Fires	1174	2.85%	Cross-terrain spread driven by extreme drought/strong winds
Pure Agricultural Fires	2110	5.12%	Interior of pure agricultural planting area
Sloping Cropland Escaped Fires	2192	5.32%	Mid-mountain steep slope zones (typical mid-elevation agricultural reclamation areas)
Persistent Smoldering in Deep Forests	1955	4.74%	Deep within old-growth dense forests with high above-ground AGB (AGB > 80 t/ha)
Wildland-Urban Interface (WUI) Fires	1244	3.02%	Urbanization expansion edges & hidden settlements in incised valleys
Topographic & Alpine Fires	1702	4.13%	Wind corridors in steep canyons & high-altitude meadows
Fires in Other Landforms	1595	3.87%	Margins of wetlands and high-alpine bare lands
Total Events	41,215	100%	

The frequency structure was dominated by two background categories: General Sporadic Forest Fires and Basin Agroforestry Ecotone Escaped Fires. These two categories accounted for 15,154 events (36.77%) and 14,089 events (34.18%), respectively, and together represented 70.95% of all reconstructed FFEs. However, their combined contributions to physical fire impact were markedly lower than their frequency share. Together, they contributed 44.36% of total burned area, 35.56% of total CFRP, and 45.34% of total AGB loss. This contrast is also evident in Figure S5a–d, where these categories dominate annual event counts but do not dominate annual shares of burned area, power release, or affected AGB in the same proportion.

By contrast, Explosive Forest Fires represented the clearest concentration of high-impact fire behavior. Although this category comprised only 1174 events (2.85% of the total), it contributed 23.12% of total burned area, 37.60% of total CFRP, and 29.61% of total AGB loss. Figure S5 further shows the annual contributions of the nine fire typologies to FFE frequency, BA, CFRP, and affected AGB. In particular, Figure S5b–d show that Explosive Forest Fires, despite their consistently low annual frequency, repeatedly occupied a disproportionately large share of annual burned area, annual power release, and annual AGB loss. These results indicate that a very small subset of forest fires dominated the regional power budget and a substantial fraction of AGB loss.

A second low-frequency but high-consequence pathway was identified for Persistent Smoldering in Deep Forests. This category represented 1955 events (4.74%), but contributed 6.42% of total burned area, 10.68% of total CFRP, and 9.22% of total AGB loss. A related contrast was observed between Pure Agricultural Fires and Sloping Cropland Escaped Fires, which accounted for 2110 events (5.12%) and 2192 events (5.32%), respectively. Although the two categories had similar event shares, the latter contributed more strongly to AGB-related impact, consistent with the higher AGB-loss ratio reported above.

The remaining categories also showed distinct physical profiles. Wildland–Urban Interface (WUI) Fires accounted for 1244 events (3.02%), with 2.49% of total burned area and 2.31% of total CFRP, indicating a limited regional share but continued management relevance because of their proximity to settlements. Topographic & Alpine Fires represented 1701 events (4.13%), 3.49% of total burned area, and 3.68% of total CFRP, indicating a moderate but terrain-specific role concentrated in steep canyon and high-elevation settings. Notably, Fires in Other Landforms accounted for 1596 events (3.87%), yet contributed 17.46% of total burned area and 9.24% of total AGB loss, indicating a distinct spread-dominated impact profile relative to their event share.

4. Discussion

4.1. Spatial Heterogeneity and Event-Level Interpretation

Taken together, the findings reveal, to some extent, the marked temporal, spatial, and topographic heterogeneity of forest fire activity in Yunnan Province, while also indicating a significant mismatch between the frequency of forest fire events and their actual impacts. Therefore, the core contribution of this study lies at the methodological level: rather than relying solely on raw hotspot counts, the analysis reconstructs physically independent FFEs by combining optical-thermal cross-validation, multi-source spatiotemporal clustering, and event-level morphological reconstruction.

This approach is particularly valuable in highly fragmented mountainous environments such as Yunnan. In such settings, raw AFS records are influenced by cross-sensor differences, geometric distortion, repeated observation of the same fire, and the coexistence of usable and unusable detections [17,21,26,31]. By reconstructing events rather than counting detections, the framework links BA, CFRP, AGB loss, persistence, and habitat context to the same analytical unit. This makes it possible to interpret regional fire heterogeneity in

a way that is more physically coherent and more useful for management than pixel-level AFS statistics alone.

The typology validation results further support the value of this event-level framework. Random Forest evaluation showed high class separability, whereas the first two principal components explained only part of the total variance [32,33]. This combination indicates that the nine fire typologies are reproducible, but also that their structure remains genuinely multidimensional. In practical terms, the typology system is not merely a visual partition of events; it summarizes differences in duration, BA, CFRP, AGB loss, LCT, and topographic position.

At the same time, the framework should not be interpreted as eliminating all sources of uncertainty. Polar-orbiting satellites still observe fires discontinuously, and the operational persistence thresholds remain partly constrained by revisit structure. Event-level reconstruction therefore improves comparability and physical interpretability, but it does not remove the need to interpret persistence, nocturnal burning, and short-lived ignitions in light of the underlying observation system [27,28].

4.2. Temporal Structure of Fire Activity and Event Consequence

The temporal results indicate that fire activity in Yunnan is organized more by concentration and consequence than by event counts alone. The late dry season was clearly the dominant annual window of fire activity [13,20,34]. Its significance lies not only in high event density, but also in the concentration of CFRP and AGB loss within the same period. Even in high-fire years, the seasonal peak intensified mainly within the usual spring fire window rather than extending greatly into other parts of the year. This suggests that interannual variation was expressed more through intensification of the established high-risk period than through a major shift in seasonal timing [9,13].

The secondary peak in autumn biomass loss is also noteworthy. Although its magnitude is far smaller than the spring peak, this suggests that the annual cycle of fire impacts does not strictly follow a unimodal distribution. A cautious interpretation is that this autumn signal arises from a combination of post-monsoon fuel drying and ongoing human activities in agricultural landscapes; however, the current dataset is better suited to identifying this pattern than to precisely quantifying the causal contributions of these processes. Therefore, it is more appropriate to retain the autumn signal as an empirical feature in the reconstructed event database and to interpret its mechanisms conservatively.

The diurnal results point to a second layer of temporal organization. Daytime burning remained dominant overall, yet nighttime activity became substantially more important in some years and near the end of the spring fire season [27,28]. The rise of nocturnal events to 20.7% in 2023 shows that interannual variation was not limited to how many fires occurred, but also affected when fires burned and how power was distributed across the day–night cycle. This is important because the increase in nocturnal median CFRP and the extension of the upper tail of nighttime power indicate that some of the most consequential fires were not confined to daytime burning windows [27,28,31].

Persistence provides a third temporal dimension. Under the 2012–2017 framework, the 105 min threshold separated a dominant short-duration group from a smaller but much more energetic persistent subset. Under the 2018–2024 framework, the 75 min threshold captured a broader range of post-ignition behavior, so the contrast between threshold classes became weaker. The most defensible interpretation is therefore not that one universal threshold defines all high-risk fires, but that long-duration events repeatedly occupy the upper tail of regional fire consequence, while the exact operational partition is partly shaped by the observation system [21,26]. The AGB results reinforce this point:

affected AGB increased strongly and non-linearly with duration, indicating that longer-lasting events were often physically larger and ecologically more consequential.

4.3. Regional Heterogeneity, Topography, and Human-Modified Landscapes

The spatial results show that Yunnan's fire regime cannot be summarized using frequency alone [29,31,35]. Southeast and Southwest Yunnan concentrated the majority of reconstructed events, yet their mean CFRP per event remained comparatively low. By contrast, Northwest and Central Yunnan contributed far fewer events but showed much higher mean CFRP per event. This means that the regional pattern of fire occurrence and the regional pattern of event-level consequence were not distributed proportionally across the province. A region with many fires was not necessarily the region where individual events were most consequential.

The typology analysis reinforces this mismatch. Background fire categories dominated event counts, but a smaller set of fire types contributed disproportionately to BA, CFRP, and AGB loss. This is one of the most important empirical findings of the study because it shows that management priority cannot be inferred directly from frequency statistics alone [30]. Recurrent background fires shape the numerical structure of the regional regime, whereas a much smaller number of high-impact fire types account for a disproportionate share of regional damage.

Topography mediates this heterogeneity in two important ways [29,36]. First, fire energy was concentrated in a limited range of slope–aspect settings, especially on gentle-to-moderate slopes under the four cardinal aspects. Second, the strongest elevational contrast was diurnal rather than interannual: nighttime fires were centered 215.03 m higher than daytime fires, whereas the difference between extreme drought years and normal years was not statistically significant. This is an important correction relative to the older version of the manuscript. The current data do not support a strong claim of systematic drought-driven upward migration of fire activity at the annual scale. What they do support is a structured topographic concentration of fire energy and a clear day–night elevational separation, consistent with recent evidence that nighttime fire behavior can play an important role in fire persistence and impact [27,28].

The interaction between topography and human-modified landscapes is especially relevant for management. The comparison between sloping cropland escaped fires and fires confined to flatter agricultural interiors suggests that similar anthropogenic ignition sources can produce very different ecological consequences once fire spreads onto steeper forest–agriculture boundaries. The underlying empirical point remains strong: the AGB loss associated with sloping cropland escaped fires was substantially higher, approximately three times that of pure agricultural fires. Likewise, deeply incised valleys and settlement-adjacent landscapes deserve specific attention because terrain complexity, response difficulty, and the potential for uphill spread can combine to increase risk even when such categories do not dominate provincial event totals [37,38].

4.4. Management Implications

The practical implication of these results is that forest fire management in Yunnan should move away from uniform suppression based only on event counts [30,39]. A large share of regional consequence was produced by a relatively small subset of high-impact events, whereas many recurrent fires remained limited in size and power. A more useful management approach is therefore to combine event frequency, expected impact, and landscape setting when prioritizing prevention and response.

In southern basin margins and agroforestry ecotones, where recurrent escaped fires account for a large share of total events, the immediate priority should be ignition prevention.

These areas require stricter seasonal control of field burning, rapid suppression of small escaped fires before they spread into adjacent vegetation, and closer monitoring during both the main spring fire peak and the smaller autumn peak. In flat agricultural interiors, the main problem is frequent occurrence; in sloping cropland and adjacent forest–agriculture boundaries, the same ignition pathway can produce much larger AGB loss. Prevention resources should therefore not be distributed evenly across all agricultural settings, but weighted toward those where escaped spread is most likely to generate broader ecological damage [29,36].

In Central and Northwest Yunnan, where event frequency is lower but mean CFRP per event is much higher, management should focus more strongly on high-impact fire pathways. In these landscapes, fuel continuity, early detection, rapid initial attack under severe drought, and strategically placed fuel breaks are likely to be more important than uniform suppression effort across all fire types. Conifer-dominated uplands and high-biomass forest stands deserve particular attention because they are more likely to support persistent or high-power burning. The practical goal in these settings is not merely reducing the number of ignitions, but preventing the relatively small number of events that account for a disproportionate share of regional impact.

Deeply incised valleys and settlement-adjacent landscapes also require targeted protection. Although these environments do not dominate provincial event totals, they combine terrain complexity, response difficulty, and the potential for uphill spread toward human infrastructure. Pre-positioned fuel breaks, terrain-specific monitoring, and locally adapted emergency planning are therefore especially important in these areas [37]. This is where the typology framework becomes operationally useful: it highlights not only which events are frequent, but also which landscape settings are likely to generate asymmetric risk relative to their frequency share.

Management priorities should also vary between normal years and extreme drought years. In normal years, prevention may focus more on recurrent agricultural spillover and routine ignition control. In extreme drought years, however, a greater share of effort should be directed toward fires with high spread potential, prolonged duration, and greater expected ecological consequence [27,28]. Under such conditions, resource allocation should shift toward early warning, rapid response, and the protection of landscapes where fuel continuity and topographic exposure can amplify event-level impact.

4.5. Limitations, Transferability, and Future Directions

Several limitations remain important. First, anthropogenic influence is inferred mainly through habitat context rather than direct behavioral, mobility, or socioeconomic data. As a result, the framework can identify recurrent agricultural spillover pathways and landscape settings associated with human activity, but it cannot yet resolve the relative importance of specific ignition practices in real time [20,37]. Second, the meteorological interpretation remains indirect because high-resolution mountain weather observations are limited, especially for local wind, humidity, temperature, and atmospheric stability in valleys and upper slopes. Third, although event-level reconstruction substantially improves the physical coherence of fire records, it still depends on discontinuous polar-orbiting observations and therefore cannot fully resolve within-event fluctuations between overpasses.

These limitations point directly to future methodological development. The framework should not only integrate higher-frequency satellite observations, but also expand the range of explanatory variables used to interpret and predict event-level fire behavior. More detailed meteorological inputs, including wind, humidity, temperature, drought severity, and local atmospheric stability, would improve the interpretation of persistence, nocturnal burning, and spread conditions in complex terrain [4,8]. Human-related variables such

as road networks, built-up areas, settlement proximity, and other indicators of access and ignition pressure would help clarify ignition pathways and landscape-specific fire pressure. Future work should also distinguish live and dead fuels more explicitly, because these two fuel components may differ substantially in seasonal dynamics, moisture sensitivity, and contribution to event intensity.

Methodologically, the framework could also be strengthened by introducing machine learning and deep learning into several stages of the workflow, including event detection, burn-scar reconstruction, typology refinement, and fire-impact prediction [12–14,32]. Such approaches may be especially useful when handling larger constellations of multi-source optical and thermal observations together with topographic, meteorological, fuel, and anthropogenic variables. At the same time, the current fire typologies should be further refined and clarified, and the parameter settings used in clustering and classification should be calibrated locally rather than assumed to be universally fixed.

The proposed event-level reconstruction framework is potentially transferable to other geographically complex fire-prone regions, but such transferability should be understood at the workflow level rather than as direct one-to-one replication. The core logic of optical–thermal cross-validation, event-level reconstruction, and multi-source spatio-temporal clustering is broadly applicable wherever fragmented landscapes and discontinuous satellite observations complicate hotspot-based fire statistics [21,24,25]. However, clustering thresholds, terrain-related constraints, and some typology rules will need local calibration according to regional fire regimes, land-cover structure, vegetation height, and sensor observation conditions. In this sense, the nine fire typologies proposed here are best viewed not as universally fixed categories, but as a transferable analytical template for comparing fire environments in fragmented and topographically complex regions.

This point is especially relevant for emerging fire-prone environments outside the subtropical mountain context of Yunnan. Warming pan-Arctic regions are experiencing increasing tundra greenness and shrub expansion, including the spread of low and taller shrubs into landscapes formerly dominated by sparse tundra vegetation, and these areas are attracting growing attention in wildfire research. For event-level reconstruction, such environments offer both opportunity and challenge: the framework may be useful in low-stature vegetation mosaics, shrub-tundra, boreal–tundra transition zones, and peat-affected landscapes, but event typologies and clustering thresholds would need recalibration because fuel continuity, vegetation stature, combustion behavior, and surface–subsurface fire coupling differ substantially from those in Yunnan's forested mountains.

An additional future direction is to improve temporal sampling while preserving long-term record continuity through renewed satellite integration. The current VIIRS constellation, including Suomi-NPP, NOAA-20, and NOAA-21, can substantially reduce revisit gaps relative to earlier VIIRS configurations and support repeat observations of the same thermal anomaly on an approximately two-hour timescale, improving the characterization of short-lived ignitions, nocturnal persistence, and within-event temporal variability [21,31]. At the same time, the long MODIS archive remains essential for preserving the historical continuity of active-fire records, even as Terra and Aqua approach the end of operations. A useful future direction is therefore to explicitly harmonize the MODIS archive with the VIIRS era, so that the historical value of MODIS can be retained while benefiting from denser temporal sampling in the post-MODIS transition.

5. Conclusions

This study developed an event-level reconstruction framework for forest fire analysis in Yunnan Province by combining optical–thermal cross-validation with multi-source spatio-temporal clustering and morphological reconstruction. Starting from 497,834 raw

AFSs detected during 2012–2024, the framework filtered unusable detections, aggregated the retained observations, and identified 41,215 validated FFEs. This event-level approach provides a more robust analytical basis than AFS counts alone for linking FFEs occurrence with BA, CFRP, AGB loss, persistence, and landscape context.

The reconstructed FFEs database reveals a strong spatiotemporal concentration of fire activity toward the end of the dry season, with 32.8% of events occurring during the primary spring fire window. Daytime events dominate the record, but in certain years, nighttime activity becomes particularly significant, accounting for as much as 20.7% in 2023. Under both observational frameworks, event durations exhibited a long-tail distribution, although operational thresholds differed between the 2012–2017 and 2018–2024 periods. Affected biomass increased significantly with longer-duration FFEs, indicating that longer-duration events are associated with more severe ecological consequences.

The spatial and topographic results further showed that event frequency and event-level impact were not distributed uniformly across Yunnan. Southeast and Southwest Yunnan concentrated most reconstructed events, whereas Northwest and Central Yunnan showed much higher CFRP per event. Fire power was concentrated mainly on gentle-to-moderate slopes, and nighttime fires were centered 215.03 m higher than daytime fires, whereas the elevational difference between extreme drought years and normal years was not statistically significant. These results indicate that Yunnan's fire regime is best described by combining occurrence frequency, event intensity, persistence, and topographic setting rather than by using fire counts alone.

The typology analysis showed that background fire categories dominated event counts, whereas a smaller subset of high-impact fire types contributed disproportionately to BA, CFRP, and AGB loss. Together, these findings demonstrate that event-level reconstruction provides a more differentiated and management-relevant understanding of forest fire heterogeneity in mountainous agroforestry environments. More broadly, the framework offers a useful foundation for both zone-specific fire management in Yunnan and future methodological application in other complex fire-prone regions.

Supplementary Materials: The following supporting information can be downloaded at: https://www.mdpi.com/article/10.3390/rs18091359/s1, Figure S1: Schematic flowchart of the MST-DBSCAN algorithm; Figure S2: Annual CFRP contribution of threshold-based persistence classes in Yunnan Province during 2012–2024; Figure S3: Annual distribution of standardized combustion persistence in Yunnan Province during 2012–2024; Figure S4: Annual odds ratio of threshold exceedance for nighttime versus daytime ignitions in Yunnan Province during 2012–2024; Figure S5: Annual contributions of the nine fire typologies to FFE frequency, BA, CFRP, and affected AGB in Yunnan Province during 2012–2024.

Author Contributions: Conceptualization, H.D. and F.Z.; methodology, H.D. and F.Z.; software, H.D., L.W. and J.Z.; validation, H.D., L.W. and J.Z.; formal analysis, H.D. and L.W.; investigation, H.D.; resources, F.Z.; data curation, H.D. and L.W.; writing—original draft preparation, H.D.; writing—review and editing, F.Z.; visualization, H.D.; supervision, F.Z.; project administration, F.Z.; funding acquisition, F.Z. All authors have read and agreed to the published version of the manuscript.

Funding: This study was financially supported by the Yunnan Fundamental Research Projects, China (Grant No. 202301AT070223); the Yunnan Reserve Projects for Young and Middle-Aged Academic and Technological Leading Talent (Grant No. 202405AC350034); the National Natural Science Foundation of China (Grant No. 32160374).

Data Availability Statement: The datasets generated during the current study are available from the corresponding author on reasonable request. The code generated during this study may be obtained from the corresponding author upon reasonable request.

Acknowledgments: The authors would like to thank the anonymous reviewers for their constructive comments and valuable suggestions, which significantly improved this paper.

Conflicts of Interest: The authors declare no conflict of interest.

Appendix A

Table A1. Annual statistics of multi-source AF data: From spatiotemporal reconstruction to validated FFEs (2012–2024).

Year	Raw Pixels (Input)				Clustered Events (Process)						Validated (Output)
	MODIS	S-NPP	NOAA -20	Input _Total	1-ISO	1-CLU	2-II	3-CI	4-CC	Process _Total	Final
2012	8758	36,773	-	45,531	2438	492	1031	1072	87	5120	4192
2013	7465	33,719	-	41,184	1514	362	615	781	88	3360	2880
2014	9558	39,880	-	49,438	3195	549	1351	1220	90	6405	5388
2015	4632	21,719	-	26,351	1392	317	578	567	50	2904	2590
2016	4617	19,429	-	24,046	1447	246	599	622	33	2947	2605
2017	3216	15,821	-	19,037	922	170	367	327	27	1813	1562
2018	3560	17,432	5628	26,620	1137	195	454	399	42	2227	1862
2019	4840	22,673	22,616	50,129	1650	264	895	941	40	3790	3175
2020	3895	15,975	16,097	35,967	1213	164	623	594	35	2629	2204
2021	4091	17,635	18,227	39,953	870	118	535	612	37	2172	1882
2022	2722	11,535	12,192	26,449	3215	420	863	642	49	5189	4770
2023	7475	32,843	32,112	72,430	3150	319	1845	1469	54	6837	6030
2024	5345	17,810	17,544	40,699	1149	187	503	584	33	2456	2075
Total	70,174	303,244	124,416	497,834	23,292	3803	10,259	9830	665	47,849	41,215

Note: Input: Raw AF pixels from MODIS and VIIRS. Process: Fire events reconstructed via MST-DBSCAN. Topological types include 1_SINGLE_ISO (isolated), 1_SINGLE_CLU (single-source cluster), 2_ISO_ISO & 3_CLU_ISO (cross-sensor fusion), and 4_CLU_CLU (multi-source intersection). Output: Final FFEs validated by morphological BA matching.

Table A2. Comparative Statistics of Sensor Confidence Profiles Between Retained and Discarded AFSs (2012–2024).

Year	Retained Pixels								Discarded Pixels							
	MODIS				VIIRS				MODIS				VIIRS			
	Tot	H	N	L	Tot	H	N	L	Tot	H	N	L	Tot	H	N	L
2012	1858	393 (21.2%)	1393 (75.0%)	72 (3.9%)	2402	72 (3.0%)	2131 (88.7%)	199 (8.3%)	395	54 (13.7%)	325 (82.3%)	16 (4.1%)	1002	15 (1.5%)	877 (87.5%)	110 (11.0%)
2013	1312	325 (24.8%)	930 (70.9%)	57 (4.3%)	1596	66 (4.1%)	1408 (88.2%)	122 (7.6%)	195	24 (12.3%)	162 (83.1%)	9 (4.6%)	491	10 (2.0%)	437 (89.0%)	44 (9.0%)
2014	2195	416 (19.0%)	1681 (76.6%)	98 (4.5%)	3373	129 (3.8%)	3005 (89.1%)	239 (7.1%)	361	49 (13.6%)	293 (81.2%)	19 (5.3%)	1313	26 (2.0%)	1166 (88.8%)	121 (9.2%)
2015	1057	190 (18.0%)	832 (78.7%)	35 (3.3%)	1547	50 (3.2%)	1369 (88.5%)	128 (8.3%)	137	19 (13.9%)	115 (83.9%)	3 (2.2%)	368	10 (2.7%)	324 (88.0%)	34 (9.2%)
2016	1089	192 (17.6%)	859 (78.9%)	38 (3.5%)	1583	53 (3.3%)	1439 (90.9%)	91 (5.7%)	161	18 (11.2%)	136 (84.5%)	7 (4.3%)	502	5 (1.0%)	461 (91.8%)	36 (7.2%)
2017	649	111 (17.1%)	514 (79.2%)	24 (3.7%)	935	32 (3.4%)	834 (89.2%)	69 (7.4%)	92	2 (2.2%)	86 (93.5%)	4 (4.3%)	246	6 (2.4%)	221 (89.8%)	19 (7.7%)
2018	699	129 (18.5%)	548 (78.4%)	22 (3.1%)	1190	52 (4.4%)	1042 (87.6%)	96 (8.1%)	125	14 (11.2%)	107 (85.6%)	4 (3.2%)	449	5 (1.1%)	404 (90.0%)	40 (8.9%)
2019	1042	229 (22.0%)	765 (73.4%)	48 (4.6%)	2140	76 (3.6%)	1870 (87.4%)	194 (9.1%)	189	21 (11.1%)	153 (81.0%)	15 (7.9%)	755	23 (3.0%)	661 (87.5%)	71 (9.4%)
2020	716	153 (21.4%)	541 (75.6%)	22 (3.1%)	1510	59 (3.9%)	1350 (89.4%)	101 (6.7%)	118	14 (11.9%)	97 (82.2%)	7 (5.9%)	547	8 (1.5%)	501 (91.6%)	38 (6.9%)
2021	695	160 (23.0%)	509 (73.2%)	26 (3.7%)	1209	61 (5.0%)	1052 (87.0%)	96 (7.9%)	103	12 (11.7%)	85 (82.5%)	6 (5.8%)	443	14 (3.2%)	384 (86.7%)	45 (10.2%)
2022	1132	101 (8.9%)	959 (84.7%)	72 (6.4%)	3652	56 (1.5%)	3358 (91.9%)	238 (6.5%)	106	4 (3.8%)	96 (90.6%)	6 (5.7%)	726	7 (1.0%)	669 (92.1%)	50 (6.9%)
2023	1697	338 (19.9%)	1278 (75.3%)	81 (4.8%)	4421	142 (3.2%)	3887 (87.9%)	392 (8.9%)	276	31 (11.2%)	231 (83.7%)	14 (5.1%)	1806	28 (1.6%)	1582 (87.6%)	196 (10.9%)
2024	762	171 (22.4%)	562 (73.8%)	29 (3.8%)	1321	45 (3.4%)	1203 (91.1%)	73 (5.5%)	178	14 (7.9%)	154 (86.5%)	10 (5.6%)	358	4 (1.1%)	327 (91.3%)	27 (7.5%)

Note: Retained/Discarded: Pixels kept or filtered out based on BA morphological validation. Confidence: Classified per NASA FIRMS as High (≥80%/h), Nominal (30–79%/n), and Low (<30%/L) for MODIS/VIIRS. Percentages denote relative proportions within each sensor and retention group.

References

1. Van Der Werf, G.R.; Randerson, J.T.; Giglio, L.; Van Leeuwen, T.T.; Chen, Y.; Rogers, B.M.; Mu, M.; Van Marle, M.J.E.; Morton, D.C.; Collatz, G.J.; et al. Global fire emissions estimates during 1997–2016. *Earth Syst. Sci. Data* **2017**, *9*, 697–720. [CrossRef]
2. Bowman, D.M.J.S.; Kolden, C.A.; Abatzoglou, J.T.; Johnston, F.H.; Van Der Werf, G.R.; Flannigan, M. Vegetation fires in the Anthropocene. *Nat. Rev. Earth Environ.* **2020**, *1*, 500–515. [CrossRef]
3. Friedlingstein, P.; O'Sullivan, M.; Jones, M.W.; Andrew, R.M.; Bakker, D.C.E.; Hauck, J.; Landschützer, P.; Le Quéré, C.; Luijkx, I.T.; Peters, G.P.; et al. Global Carbon Budget 2023. *Earth Syst. Sci. Data* **2023**, *15*, 5301–5369. [CrossRef]
4. Abatzoglou, J.T.; Williams, A.P.; Boschetti, L.; Zubkova, M.; Kolden, C.A. Global patterns of interannual climate–fire relationships. *Glob. Change Biol.* **2018**, *24*, 5164–5175. [CrossRef]
5. Pausas, J.G.; Keeley, J.E. Wildfires and global change. *Front. Ecol. Environ.* **2021**, *19*, 387–395. [CrossRef]
6. Jolly, W.M.; Cochrane, M.A.; Freeborn, P.H.; Holden, Z.A.; Brown, T.J.; Williamson, G.J.; Bowman, D.M.J.S. Climate-induced variations in global wildfire danger from 1979 to 2013. *Nat. Commun.* **2015**, *6*, 7537. [CrossRef]
7. Andela, N.; Morton, D.C.; Giglio, L.; Chen, Y.; Van Der Werf, G.R.; Kasibhatla, P.S.; DeFries, R.S.; Collatz, G.J.; Hantson, S.; Kloster, S.; et al. A human-driven decline in global burned area. *Science* **2017**, *356*, 1356–1362. [CrossRef]
8. Jones, M.W.; Abatzoglou, J.T.; Veraverbeke, S.; Andela, N.; Lasslop, G.; Forkel, M.; Smith, A.J.P.; Burton, C.; Betts, R.A.; van der Werf, G.R.; et al. Global and regional trends and drivers of fire under climate change. *Rev. Geophys.* **2022**, *60*, e2020RG000726. [CrossRef]
9. Deng, X.; Li, J.; Dai, X.; Zhao, J.; Deng, H.; Zhao, F. Predicting dynamics of wildfire regimes in yunnan, china. *Discov. Appl. Sci.* **2024**, *6*, 99. [CrossRef]
10. Cui, L.; Luo, C.; Yao, C.; Zou, Z.; Wu, G.; Li, Q.; Wang, X. The influence of climate change on forest fires in yunnan province, southwest China detected by GRACE satellites. *Remote Sens.* **2022**, *14*, 712. [CrossRef]
11. Yuan, Z.; Wu, D.; Wang, T.; Ma, X.; Li, Y.; Shao, S.; Zhang, Y.; Zhou, A. Holocene fire history in southwestern China linked to climate change and human activities. *Quat. Sci. Rev.* **2022**, *289*, 107615. [CrossRef]
12. Chen, Y.; Kou, W.; Miao, W.; Yin, X.; Gao, J.; Zhuang, W. Mapping burned forest areas in western yunnan, china, using multi-source optical imagery integrated with simple non-iterative clustering segmentation and random forest algorithms in Google earth engine. *Remote Sens.* **2025**, *17*, 741. [CrossRef]
13. Zhang, H.; Wang, W.; Ban, Q. Seasonal forest fire risk and key drivers in Yunnan Province: A machine learning approach. *npj Nat. Hazards* **2025**, *2*, 59. [CrossRef]
14. Xu, Z.; Li, J.; Cheng, S.; Rui, X.; Zhao, Y.; He, H.; Guan, H.; Sharma, A.; Erxleben, M.; Chang, R. Deep learning for wildfire risk prediction: Integrating remote sensing and environmental data. *ISPRS J. Photogramm. Remote Sens.* **2025**, *227*, 632–677. [CrossRef]
15. Fu, Y.; Li, R.; Wang, X.; Bergeron, Y.; Valeria, O.; Chavardès, R.D.; Wang, Y.; Hu, J. Fire Detection and Fire Radiative Power in Forests and Low-Biomass Lands in Northeast Asia: MODIS versus VIIRS Fire Products. *Remote Sens.* **2020**, *12*, 2870. [CrossRef]
16. Fornacca, D.; Ren, G.; Xiao, W. Performance of Three MODIS Fire Products (MCD45A1, MCD64A1, MCD14ML), and ESA Fire_CCI in a Mountainous Area of Northwest Yunnan, China, Characterized by Frequent Small Fires. *Remote Sens.* **2017**, *9*, 1131. [CrossRef]
17. Giglio, L.; Schroeder, W.; Justice, C.O. The collection 6 MODIS active fire detection algorithm and fire products. *Remote Sens. Environ.* **2016**, *178*, 31–41. [CrossRef]
18. Long, T.; Zhang, Z.; He, G.; Jiao, W.; Tang, C.; Wu, B.; Zhang, X.; Wang, G.; Yin, R. 30 m Resolution Global Annual Burned Area Mapping Based on Landsat Images and Google Earth Engine. *Remote Sens.* **2019**, *11*, 489. [CrossRef]
19. Yang, J.; Huang, X. The 30 m annual land cover dataset and its dynamics in China from 1990 to 2019. *Earth Syst. Sci. Data* **2021**, *13*, 3907–3925. [CrossRef]
20. Ying, L.; Cheng, H.; Shen, Z.; Guan, P.; Luo, C.; Peng, X. Relative humidity and agricultural activities dominate wildfire ignitions in Yunnan, Southwest China: Patterns, thresholds, and implications. *Agric. For. Meteorol.* **2021**, *307*, 108540. [CrossRef]
21. Schroeder, W.; Oliva, P.; Giglio, L.; Csiszar, I.A. The New VIIRS 375 m active fire detection data product: Algorithm description and initial assessment. *Remote Sens. Environ.* **2014**, *143*, 85–96. [CrossRef]
22. Giglio, L.; Boschetti, L.; Roy, D.P.; Humber, M.L.; Justice, C.O. The Collection 6 MODIS burned area mapping algorithm and product. *Remote Sens. Environ.* **2018**, *217*, 72–85. [CrossRef]
23. Wooster, M.J.; Roberts, G.; Perry, G.L.W.; Kaufman, Y.J. Retrieval of biomass combustion rates and totals from fire radiative power observations: FRP derivation and calibration relationships between biomass consumption and fire radiative energy release. *J. Geophys. Res. Atmos.* **2005**, *110*, 2005JD006318. [CrossRef]
24. Roteta, E.; Bastarrika, A.; Padilla, M.; Storm, T.; Chuvieco, E. Development of a Sentinel-2 burned area algorithm: Generation of a small fire database for sub-Saharan Africa. *Remote Sens. Environ.* **2019**, *222*, 1–17. [CrossRef]
25. Kurbanov, E.; Vorobev, O.; Lezhnin, S.; Sha, J.; Wang, J.; Li, X.; Cole, J.; Dergunov, D.; Wang, Y. Remote sensing of forest burnt area, burn severity, and post-fire recovery: A review. *Remote Sens.* **2022**, *14*, 4714. [CrossRef]

26. Csiszar, I.; Schroeder, W.; Giglio, L.; Ellicott, E.; Vadrevu, K.P.; Justice, C.O.; Wind, B. Active fires from the Suomi NPP Visible Infrared Imaging Radiometer Suite: Product status and first evaluation results. *J. Geophys. Res. Atmos.* **2014**, *119*, 803–816. [CrossRef]
27. Balch, J.K.; Abatzoglou, J.T.; Joseph, M.B.; Koontz, M.J.; Mahood, A.L.; McGlinchy, J.; Cattau, M.E.; Williams, A.P. Warming weakens the night-time barrier to global fire. *Nature* **2022**, *602*, 442–448. [CrossRef] [PubMed]
28. Luo, K.; Wang, X.; De Jong, M.; Flannigan, M. Drought triggers and sustains overnight fires in North America. *Nature* **2024**, *627*, 321–327. [CrossRef] [PubMed]
29. Li, W.; Xu, Q.; Yi, J.; Liu, J. Predictive model of spatial scale of forest fire driving factors: A case study of Yunnan Province, China. *Sci. Rep.* **2022**, *12*, 19029. [CrossRef]
30. Szpakowski, D.M.; Jensen, J.L.R. A Review of the Applications of Remote Sensing in Fire Ecology. *Remote Sens.* **2019**, *11*, 2638. [CrossRef]
31. Wooster, M.J.; Roberts, G.J.; Giglio, L.; Roy, D.P.; Freeborn, P.H.; Boschetti, L.; Justice, C.; Ichoku, C.; Schroeder, W.; Davies, D.; et al. Satellite remote sensing of active fires: History and current status, applications and future requirements. *Remote Sens. Environ.* **2021**, *267*, 112694. [CrossRef]
32. Belgiu, M.; Drăguţ, L. Random forest in remote sensing: A review of applications and future directions. *ISPRS J. Photogramm. Remote Sens.* **2016**, *114*, 24–31. [CrossRef]
33. Pelletier, C.; Valero, S.; Inglada, J.; Champion, N.; Dedieu, G. Assessing the robustness of Random Forests to map land cover with high resolution satellite image time series over large areas. *Remote Sens. Environ.* **2016**, *187*, 156–168. [CrossRef]
34. Luo, K.; Quan, X.; He, B.; Yebra, M. Effects of Live Fuel Moisture Content on Wildfire Occurrence in Fire-Prone Regions over Southwest China. *Forests* **2019**, *10*, 887. [CrossRef]
35. Deng, H.; Li, D.; Cai, S.; Zhao, F.; Zhao, J. Spatio-temporal dynamics of forest fire occurrence in Yunnan, China from 2001 to 2021 based on MODIS. *npj Nat. Hazards* **2025**, *2*, 52. [CrossRef]
36. Zhai, J.; Ning, Z.; Dahal, R.; Yang, S. Wildfire susceptibility of land use and topographic features in the Western United States: Implications for the landscape management. *Forests* **2023**, *14*, 807. [CrossRef]
37. Radeloff, V.C.; Helmers, D.P.; Kramer, H.A.; Mockrin, M.H.; Alexandre, P.M.; Bar-Massada, A.; Butsic, V.; Hawbaker, T.J.; Martinuzzi, S.; Syphard, A.D.; et al. Rapid growth of the US wildland-urban interface raises wildfire risk. *Proc. Natl. Acad. Sci. USA* **2018**, *115*, 3314–3319. [CrossRef] [PubMed]
38. Moritz, M.A.; Batllori, E.; Bradstock, R.A.; Gill, A.M.; Handmer, J.; Hessburg, P.F.; Leonard, J.; McCaffrey, S.; Odion, D.C.; Schoennagel, T.; et al. Learning to coexist with wildfire. *Nature* **2014**, *515*, 58–66. [CrossRef]
39. Tedim, F.; Leone, V.; Amraoui, M.; Bouillon, C.; Coughlan, M.; Delogu, G.; Fernandes, P.; Ferreira, C.; McCaffrey, S.; McGee, T.; et al. Defining Extreme Wildfire Events: Difficulties, Challenges, and Impacts. *Fire* **2018**, *1*, 9. [CrossRef]

Disclaimer/Publisher's Note: The statements, opinions and data contained in all publications are solely those of the individual author(s) and contributor(s) and not of MDPI and/or the editor(s). MDPI and/or the editor(s) disclaim responsibility for any injury to people or property resulting from any ideas, methods, instructions or products referred to in the content.